Journal of Extracellular Vesicles

RESEARCH ARTICLE OPEN ACCESS

T-Cell-Derived Exosomes From Multi Core Granules Exhibit Superior Caspase-3-Mediated Tumor-Suppressive Activity Compared to Those From Multivesicular Bodies

Nadia Alawar[1] | Claudia Schirra[1] | Ruth Rasuli[1,2] | Claudia Fecher-Trost[3,4] | Lisa Weins[1,5] | Markus R. Meyer[4] | Veit Flockerzi[3] | A. Keller[6,7,8] | Michael L. Dustin[9] | Jens Rettig[1] | Ute Becherer[1]

[1]Cellular Neurophysiology, Center for Integrative Physiology and Molecular Medicine (CIPMM), Saarland University, Homburg, Germany | [2]Department of Medical Oncology and Hematology, University Hospital of Zürich (USZ), Zürich, Switzerland | [3]Institute of Experimental and Clinical Pharmacology and Toxicology, Saarland University, Homburg, Germany | [4]Department of Experimental and Clinical Toxicology and Pharmacology, Center for Molecular Signaling (PZMS), Saarland University, Homburg, Germany | [5]Department of Hematology and Oncology, Caritas Klinikum Saarbrücken, Saarbrücken, Germany | [6]Clinical Bioinformatics, Saarland University, Saarbrücken, Germany | [7]Helmholtz Institute for Pharmaceutical Research Saarland (HIPS), Helmholtz Centre for Infection Research, Saarbrücken, Germany | [8]PharmaScienceHub, Saarbrücken, Germany | [9]Kennedy Institute of Rheumatology, Nuffield Department of Orthopaedics, Rheumatology and Musculoskeletal Sciences, University of Oxford, Oxford, UK

Correspondence: Claudia Schirra (Claudia.Schirra@uks.eu) | Ute Becherer (Ute.Becherer@uks.eu)

Received: 27 May 2025 | **Revised:** 5 December 2025 | **Accepted:** 27 January 2026

Keywords: 10X-expansion | CD8$^+$ T-cells | extracellular vesicles | immunological synapse | Munc13-4 | primary cells | multivesicular bodies | tetraspanins

ABSTRACT

Small extracellular vesicles (sEVs) derived from cytotoxic T lymphocytes (CTLs) are emerging as potential mediators of antitumor immunity; however, their subcellular origins and functional properties remain incompletely defined. In this study, we investigated the intracellular routes and cytotoxic potential of CTL-derived exosomes. Using correlative light and electron microscopy, we discovered that CTL-derived exosomes originate from both classical multivesicular bodies (MVBs) and the recently identified multi core granules (MCGs). Through total internal reflection fluorescence microscopy, we demonstrated that, in contrast to MVB-derived exosomes, MCG-derived exosomes are released at the immunological synapse in a stimulus-dependent manner. To enable functional characterization, we developed a scalable primary cell culture method for the isolation of high-purity exosomes. Super-resolution microscopy revealed significant heterogeneity in exosome size and tetraspanin composition. Notably, MCG-derived exosomes exhibited fivefold higher cytotoxic activity than MVB-derived exosomes, inducing apoptosis in tumor cells via a caspase 3-dependent mechanism. These findings reveal that CTLs exploit distinct secretory pathways to release heterogeneous exosome populations with differential cytotoxic capacities, offering new insights into CTL-mediated immune responses and providing a basis for the development of novel exosome-based immunotherapies.

1 | Introduction

Cytotoxic T lymphocytes (CTLs) are essential components of adaptive immunity, responsible for the targeted elimination of virus-infected and malignant cells. This cytotoxic activity is initiated through the formation of an immunological synapse (IS) between the CTL and its target cell, triggering a cascade of intracellular events that ultimately lead to target cell death (Chang et al. 2023; Dustin and Choudhuri, 2016; Kabanova et al., 2018). To execute this process, CTLs deploy an arsenal of effector mechanisms, including the release of cytotoxic molecules such as perforin and granzymes (Gzms) (Lopez et al. 2013; McKenzie

et al. 2022; Sutton et al. 2016), Fas ligand (Bossi and Griffiths 1999; Cassioli and Baldari 2022), and cytokines such as interferon γ (IFN-γ) (Alspach et al. 2019; Uhl et al. 2023). These effector molecules are packaged in distinct organelles, notably within lytic granules that comprise two subtypes: single core granules (SCGs) and multi core granules (MCGs) (Balint et al. 2020; Chang et al. 2022). SCGs are characterized by a homogeneous, electron-dense core and release Gzms and perforin in a soluble form, enabling rapid target cell killing. In contrast, MCGs contain multiple small electron-dense cores, known as supramolecular attack particles (SMAPs), which kill target cells (Balint et al. 2020; Chang et al. 2022). Both granule types undergo calcium-dependent fusion with the plasma membrane, exclusively at the IS (Chang et al. 2022). Their fusion is orchestrated by a specialized molecular machinery, in which the SNARE proteins together with priming/docking proteins play a central role (Chang et al. 2023). Among the priming/docking proteins, Munc13-4 plays a pivotal role by facilitating the docking of lytic granules and promoting the assembly of the SNARE complex, consisting of the v-SNARE Synaptobrevin-2 in mouse and the t-SNAREs syntaxin-11 and SNAP23 (Chang et al. 2023). Notably, Munc13-4 deletion completely abolishes the exocytosis of lytic granules at the IS of CTLs (Crozat et al. 2007; Dudenhoffer-Pfeifer et al. 2013; Feldmann et al. 2003).

In a previous study, we demonstrated that in addition to SMAPs, MCGs also harbor intraluminal vesicles (ILVs), suggesting that they may serve as a source of small extracellular vesicles (sEVs), alongside the classical multivesicular bodies (MVBs) (Peters et al. 1991). EVs constitute a heterogeneous group of membrane-bound vesicles secreted by nearly all cell types, critically mediating intercellular communication and influencing diverse physiological and pathological processes. EVs are typically categorized into exosomes, microvesicles, and apoptotic bodies, based on their size and subcellular origin. Exosomes, generally have a size range of 30–150 nm in diameter, originate as ILVs within endosomal compartments and are released upon their fusion with the plasma membrane (Raposo and Stoorvogel 2013; Welsh et al. 2024). They contain a diverse cargo of proteins, DNA, and RNA, which mediate cell-to-cell signaling. While extensive research has explored the roles of tumor-derived exosomes in immune evasion, immunosuppression, and metastasis, immune cell-derived exosomes, particularly those from CTLs, have been comparatively neglected, despite them being the key players in the fight against cancer (Budayr et al. 2025; Li et al. 2025). CTL-derived EVs have been shown to have anti-tumor properties by reducing cancer cell proliferation and metastatic properties (Budayr et al. 2025; Seo et al. 2018; Sovunjov et al. 2023; Zhang et al. 2024; Zhou et al. 2021), but also promote cancer invasion (Cai et al. 2012). Furthermore, they play a role in the modulation of the immune system by influencing the function of bystander CTLs (Li et al. 2017; Wu et al. 2019). Most research in CTLs was focused on EVs in general rather than specifically on exosomes, or have been conducted using cytotoxic cell lines (NK92), leaving significant gaps in our understanding of their cellular origin, composition, and function in primary CTLs.

In this study, we systematically address these gaps by thoroughly characterizing small EVs derived from primary murine CTLs. Specifically, we investigated their intracellular localization, release kinetics, protein composition and role in tumor suppression. Our results indicate that CTL-derived small EVs are exosomes that originate not only from classical MVBs, but also from the recently described MCGs (Chang et al. 2022), and that the latter are released specifically at the IS, in parallel with SMAPs, in a stimulus-dependent manner. We further demonstrated that the isolated exosomes exhibited remarkable heterogeneity in size and protein composition. Importantly, we observed distinct functional differences between those derived from MVBs and MCGs. MCG-derived exosomes exhibited significantly higher cytotoxic activity, effectively inducing apoptosis in tumor cells through a caspase 3-dependent mechanism. By elucidating the different origins, heterogeneity, and functionality of CTL-derived exosomes, this study significantly enhances our understanding of their biological roles and therapeutic potential.

2 | Materials and Methods

2.1 | Animal Housing and Ethical Compliance

Munc13-4 knock-out (KO) (*Unc13d*$^{-/-}$) and GzmB-mTFP knock-in (KI) mice were generated as described previously (Chitirala et al. 2020; Crozat et al. 2007). All animal experiments were conducted in accordance with the regulations of the state of Saarland (Landesamt für Verbraucherschutz, AZ.: 2.4.1.1) and approved by the appropriate authorities. Mice of both sexes were maintained under specific pathogen-free (SPF) conditions in a controlled environment at 22°C with 50%–60% humidity and a 12-h light/dark cycle. Food and water were provided ad libitum. For euthanasia, mice were anesthetized using CO_2, followed by cervical dislocation, in accordance with the AVMA Guidelines (2007).

2.2 | Cell Culture

Spleens from 18–22-week-old C57BL/6N wild-type (WT), GzmB-mTFP KI, or Munc13-4 KO mice were harvested and processed into single-cell suspensions. Briefly, CD8$^+$ T-cells were positively isolated from splenocytes of WT, KO, or KI mice using Dynabeads Flowcomp CD8 positive isolation kit (Invitrogen) following manufacturer's instructions. The naïve CD8$^+$ T cells were activated with anti-CD3/anti-CD28 coated activator beads (ratio 1:0.8) and cultured for 5 days at 37°C with 5% CO_2. The resulting CTLs were cultured at a density 10^6 cells/mL in 24 well plates with AIM-V medium (Invitrogen) containing 10% fetal calf serum (FCS), 100 U/mL recombinant IL-2 (Gibco), 50 µM 2-mercaptoethanol. For exosome isolation, 8–10 × 10^6 cells/mouse were resuspended in AIM-V medium supplemented with 10% depleted FCS (dFCS) and 50 µM β-mercaptoethanol in T75 flasks at 37°C with 5% CO_2. Cells were activated as described previously and supplemented with fresh medium containing 10% dFCS and 100 U/mL recombinant IL-2 every second day. Depleted FCS was prepared by ultracentrifugation at 100,000 × *g* at 4°C for 16 h, with the supernatant aliquoted and stored at −20°C.

P815 cells were cultured in RPMI medium (Gibco) supplemented with 10% FCS and 1% Penicillin/Streptomycin. The cells were cultured in the medium at 37°C in a humidified incubator with 5% CO_2. Cells were passaged every two days at a 1:33 ratio and used between passages 16 and 20.

2.3 | Cell Homogenization and Organelle Isolation

Cell homogenization was performed as previously described (Chang et al. 2022). Briefly, 0.8–1.5 × 10^8 day 5 CTLs from WT mice were washed in ice-cold isolation buffer (Invitrogen, PBS with 0.1% BSA and 2 mM EDTA) and centrifuged at 300 × *g* for 6 min. The pellet was resuspended in 2 mL homogenization buffer (300 mM sucrose, 10 mM HEPES, 5 mM EDTA, pH 7.3) supplemented with protease inhibitors (3 mM Pefabloc, 10 µM E64, and 10 µg Pepstatin A). Nitrogen cavitation was performed for 25 min at 4°C and 800 psi. The resulting homogenate was collected and centrifuged at 1000 × *g* for 10 min at 4°C. The post-nuclear supernatant was layered on top of a discontinuous sucrose density gradient with 0.3, 0.5, 0.8, 1.0, 1.2, 1.4, and 1.6 M sucrose in 10 mM HEPES with 5 mM EDTA with protease inhibitors as described before. Each sucrose layer consisted of 2 mL except for the 0.5 and 0.8 M sucrose layer, which was 1 mL. After ultracentrifugation at 100,000 × *g* for 90 min at 4°C in a SW40Ti rotor (Beckmann), twelve 1 mL fractions were collected from the top of the gradient and supplemented with fresh protease inhibitors.

2.4 | EV and Exosome Isolation

EV isolation was performed on day 5 effector $CD8^+$ T lymphocytes cultivated in exosome depleted FCS as described above using a differential ultracentrifugation protocol. Briefly, the supernatant from 600–800 × 10^6 from WT or Munc13-4 KO CTLs was collected and centrifuged for 10 min at 1000 × *g* and 20 min at 2000 × *g* respectively. Activation beads were collected by magnetic separation and washed thoroughly with calcium free D-PBS (Ca^{2+} and Mg^{2+} free) to recover any EVs adhering to their surface. The D-PBS used for washing the beads was then mixed with the culture supernatant before the subsequent EV isolation steps, ensuring that polarized released EVs were included in the analysis. The resulting supernatant was ultracentrifuged at 10,000 × *g* for 40 min followed by a 100,000 × *g* ultracentrifugation for 75 min. The pellet was washed with D-PBS containing a cocktail of protease inhibitors (Pefabloc, E64, Pepstatin A).

For exosome isolation, the sample was ultracentrifuged using the SW40 rotor for 75 min. All centrifugation steps were performed at 4°C. The exosome pellet was resuspended in 50 µL D-PBS and added to a sucrose density gradient with 0.3, 0.6, 0.95, 1.1, 1.2, 1.3, 1.6, and 2 M sucrose solution in 20 mM HEPES pH 7.3, 5 mM EDTA. A protease inhibitor mixture consisting of 3 mM Pefabloc, 10 µM E64, and 10 µg Pepstatin A was added to these solutions, except when the exosomes were intended for killing assays (in which case, inhibitors were omitted). The gradient was subjected to ultracentrifugation at 100,000 × *g* at 4°C for 18 h. Sucrose fractions were then collected, diluted in D-PBS, and ultracentrifuged again for 75 min at 100,000 × *g* at 4°C to further purify the exosomes. The final exosome pellet was resuspended in calcium free 50–80 µL D-PBS. Exosomes were used immediately or stored at 4°C for no more than 24 h prior to further analysis.

For differential mass spectrometry analysis of $CD63^+$ and $CD81^+$ exosomes, EVs were isolated as described above. EV pellets were resuspended in D-PBS and subjected to the mouse CD63 or mouse CD81 exosome isolation kit (Miltenyi Biotec, Germany), following the manufacturer's instructions. Briefly, EV samples were incubated with magnetic microbeads conjugated to anti-CD63 or anti-CD81 antibodies for 1 h at room temperature. The bead–EV complexes were then applied to µMACS columns placed in a magnetic separator. After extensive washing to remove unbound material, the columns were removed from the magnetic field, and bead-bound exosomes were directly lysed in Laemmli sample buffer supplemented with 10% β-mercaptoethanol. Samples were stored at -20°C for subsequent mass spectrometry.

2.5 | Plasmids Used for Transfection

Granzyme B (GzmB) -pHuji was cloned by replacing mCherry at the C-terminus of GzmB with forward primer 5′-ATG TAT ATC CAC CGG TCG CCA CCA TGG TGA GCA AGG GCG AGG AG-3′ and reverse primer 5′-ATG TAT ACT AGC TAG CTT ACT TGT ACA GCT CGT CCA TGC CGC CG-3′. Its size was 4.315 kb. The pmax-CD81-super ecliptic pHluorin (SEP) was generated by subcloning from pCMV-CD81-SEP into pMax with the restriction sites EcoRI and XbaI. Its size was 4.312 kb. The pmax-CD63-pHuji was generated by subcloning from pCMV-CD63-pHuji into pMax with the restriction sites EcoRI and XbaI. Its size was 4.282 kb. The pmax-CD63-SEP was generated by subcloning from pCMV-CD63-SEP into pMax with the restriction sites EcoRI and XbaI. Its size was 4.318 kb. pCMV-CD81-SEP, pCMV-CD63-pHuji, and pCMV-CD63-SEP were a generous gift from Frederik Verweij (Centre de Psychiatrie et neurosciences, Amsterdam/Paris). For both constructs the pH sensitive fluorescent marker protein was located to the first extracellular loop of the tetraspanins facing the acidic lumen of the organelles (Figure S1f) (Verweij et al. 2018). The pMax-CD81-Halo was cloned by replacing the SEP in the CD81-SEP with forward primer 5′- ATA TAC CGG AAT TCC ATG GGA GTG GAG G-3′ and reverse primer 5′-GAT TCG AGC TCC ACC GGT GCC GGA AAT CTC GAG CG-3′. Its size was 4.486 kb. The pMax-CD63-pHuji-Halo was generated by subcloning from pCMV-CD63-SEP into pMax with forward primer 5′-ATA TAC CGG AAT TCC ATG GCG GTG GAA GGA-3′ and reverse primer 5′-ATA TAG CTC TAG ACA TCA CCT CGT AGC CAC TTC TGA TAC-3′, then the Halo Tag was added to the generated construct with forward primer 5′-ATA TAG CTC TAG AGG TGG GAG CGG AAG CGG C-3′ and reverse primer 5′-ATA TAC GCG GAT CCT TAG CCG GAA ATC TCG AGC GTC GAC AGC CA-3′. Its size was 5.197 kb. All plasmids were confirmed by sequencing with respective forward and reverse primers by Microsynth Seqlab.

2.6 | Electroporation of CTLs

Electroporation of day 5 mouse CTLs was performed using the Nucleofector 2b Device (Lonza). Approximately 6 × 10^6 cells were resuspended in 100 µL electroporation buffer (Mouse T Cell Nucleofector Kit, VPA-1006; Lonza) and 1.5–3 µg plasmid DNA (CD63-pHuji, CD63-SEP, CD81-SEP, CD63-pHuji-Halo, CD81-Halo, or GzmB-pHuji). The cell-DNA mixture was transferred to cuvettes and electroporated with the X-001 pulse for mouse CTLs. Following electroporation, cells were transferred to 3 mL prewarmed recovery medium and cultured at 32°C with 5% CO_2 (Alawar et al. 2024). After 12 h, cells were washed, cultured in AIM-V with 10% FCS at 37°C, and used for experiments 14–18 h post-electroporation.

2.7 | Total Internal Reflection Fluorescence Microscopy (TIRFM)

The TIRFM setup (Visitron Systems GmbH, Germany) was based on an Olympus IX83 microscope, equipped with a UAPON100XOTIRF NA 1.49 objective, a 488 nm and a 561 nm 100 mW laser, and an Evolve-Prime95B camera (Teledyne Photometrics). Illumination was controlled by the iLAS2 system (Roper Scientific, France) with Semrock (USA) filters. Day 4 $CD8^+$ T cells were co-transfected with combinations of CD63-pHuji, CD81-SEP, and GzmB-pHuji. 14–18 h post-electroporation, around 0.3×10^6 cells were resuspended in 30 µL extracellular buffer (2 mM HEPES, 140 mM NaCl, 4.5 mM KCl, and 2 mM $MgCl_2$) containing 0 mM nominal Ca^{2+} and allowed to settle for 1–2 min on anti-CD3ε antibodies (30 µg/mL, clone 145-2C11, BD Pharmingen) coated coverslips. Cells were then perfused with extracellular buffer containing 10 mM Ca^{2+} to promote vesicle fusion. Imaging was performed for 10 min at room temperature, with a 10 Hz acquisition frequency and 100 ms exposure time using the 561 nm and 488 nm lasers. Fusion events were analyzed using Fiji V1.4 with the Time Series Analyzer plugin.

2.8 | Subset Analysis of $CD8^+$ T Lymphocytes by Flow Cytometry

Flow cytometry was performed to assess the quality, activation status, and differentiation of day 5 $CD8^+$ T lymphocytes. Briefly, $0.2–0.5 \times 10^6$ $CD8^+$ T cells were resuspended in D-PBS (Gibco) and incubated on ice for 30 min in the dark with FITC-, APC-, or PE-conjugated antibodies against CD44, CD62L, and CD25. Viable $CD8^+$ T cells were gated based on size and granularity, using unstained CTLs as controls. Data acquisition was performed with a BD FACSAria III analyzer and BD FACSDiva software 6.0, and analysis was conducted using FlowJo v10.0.7.

2.9 | Protein Lysates and Western Blot Analysis

Approximately 10×10^6 CTLs were lysed in RIPA buffer, incubated on ice, and centrifuged to collect the supernatant. For sucrose gradient fractions and exosome pellets, 10 µL of each sample was lysed in RIPA buffer.

Western blot analysis was used to assess protein expression. Protein lysates (10 µg) were mixed with LDS buffer and, if required, β-mercaptoethanol for reducing conditions. The samples were heated, loaded onto a 4%–12% Bis-Tris gel, and separated by SDS-PAGE. Proteins were transferred to a 0.45 µm nitrocellulose membrane. After blocking with 5% milk in TBST, membranes were incubated with primary antibodies, followed by HRP-conjugated secondary antibodies. For isolated organelles and exosomes, protein concentrations in sucrose fractions were quantified using Pierce 660 nm Protein Assay reagent. Sucrose fractions were separated by SDS-PAGE using either 10% Bis-Tris gels with MES running buffer or 4%–12% gradient Bis-Tris gels with MOPS running buffer. Proteins were transferred to a 0.2 µm pore-size nitrocellulose membrane and blocked with 5% non-fat dry milk powder in TBS buffer (20 mM Tris, 0.15 M NaCl, 0.05% Tween 20, pH 7.4) for 2 h at 20 ± 2°C. The immunoblots were probed with primary antibodies against alpha-tubulin, synaptobrevin 7, GzmB, EEA1, ALIX, TSG101, and CD81 followed by HRP-conjugated secondary antibodies (goat anti-mouse or anti-rabbit, heavy and light chain). The blots were developed using enhanced chemiluminescence (Super Signal West Dura Chemiluminescent Substrate) and imaged with a FluorChem M gel documentation system (ProteinSimple).

2.10 | Immunostaining

$CD8^+$ T cells were allowed to settle on anti-CD3ε-coated coverslips (30 µg/mL) for 10 min at room temperature and fixed with 4% paraformaldehyde for 20 min. After three washes with D-PBS, cells were permeabilized with 2% BSA and 0.1% Triton-X-100 for 30 min, followed by blocking with 2% BSA in D-PBS for 30 min. Primary antibodies (Table S1) were incubated for 1 h, followed by washing with a permeabilizing solution. Secondary antibodies (Table S1) were added for 45 min in the dark, and excess antibody was washed away three times with D-PBS. The coverslips were rinsed in distilled water and mounted immediately. All steps were performed at room temperature.

Isolated organelles in sucrose fractions were fixed with 0.2% PFA on ice for 10 min and diluted with 320 mM KCl. They were added to 2% gelatin-coated coverslips fixed in ultracentrifuge tubes and ultracentrifuged for 30 min at 10,000 × *g*. The samples were further fixed with 2% PFA for 5 min. After three washes with D-PBS and quenching with 50 mM glycine for 2 min, the primary antibody was added for 30 min at 20 ± 2°C. The secondary antibody was applied for 30 min. After several washes with D-PBS, the coverslips were dipped in distilled water and mounted on slides. For co-staining, antibodies from the same species were stained consecutively with Fab fragments in between. Samples were stored at 4°C until imaging using SIM.

Isolated exosomes were resuspended in approximately 14 mL of D-PBS, added to 2% gelatin-coated coverslips, fixed in ultracentrifuge tubes on an adapter, and ultracentrifuged at 20,000 × *g* for 4 h. Following centrifugation, the exosomes were fixed in 2% PFA for 5 min at 20 ± 2°C. The fixing solution was then removed, and exosomes were washed once with D-PBS. The sample was quenched with 2 mM glycine solution for 5 min at room temperature. After three washing steps of 5 min each, exosomes were permeabilized using 0.001% Triton-X-100 solution in D-PBS for 5 min and blocked for 10 min using blocking solution (2% BSA in D-PBS). The primary antibody (Table S1) was diluted in blocking solution and applied for 30 min at 20 ± 2°C. After two washes with blocking solution the secondary antibody (Table S1) was added for 30 min. The sample was washed three times with D-PBS and the coverslip was dipped into distilled water and mounted using mounting medium on top of a cover slide. The samples were stored at 4°C for imaging using SIM or Expansion Microscopy.

2.11 | Structured Illumination Microscopy (SIM)

The SIM imaging was performed on a Zeiss Elyra PS1 (Zeiss, Oberkochen) equipped with solid-state lasers emitting at 405

nm, 488 nm, 561 nm, and 642 nm. Post-immunostaining, images were captured using a 63× Plan-Apochromat (NA 1.4) objective with laser excitations at 488 nm, 561 nm, and 642 nm. Z-stacks were recorded with a step size of 150 nm. The raw images were processed using Zen software (Zen 2011; Carl Zeiss), and further analysis was performed using ImageJ v1.46 software. Segmentation was performed with Cellpose 2.0 (Pachitariu and Stringer 2022). Co-localization analysis was performed with JACoP in ImageJ (Bolte and Cordelieres 2006) or object based co-localization analysis using in house written macro.

For correlative light and electron microscopy (CLEM) imaging, ultrathin sections of post-embedded GzmB-mTFP KI mouse CTLs expressing CD81-Halo or CD63-Halo-pHuji, stained with SiR or ATTO647 (as described above), were imaged using 405, 488, and 642 nm wavelengths. SIM imaging with a 63× Plan-Apochromat objective (NA 1.4) covered a 200-mesh grid (around 90 μm^2), ensuring precise alignment with the grid bars. DAPI images were taken at 405 nm to identify CTL nuclei and define the image plane. Z-stacks were acquired with a step size of 100 nm, and image processing was performed using Zen 2011 (Zeiss).

2.12 | High Pressure Freezing and Electron Microscopy

To localize proteins within CTL organelles, CLEM analysis of cryo-fixed GzmB-KI mouse CTLs was conducted as previously described (Matti et al., 2013). Day 5 CTLs from GzmB-KI mice were co-transfected with CD63-pHuji and CD81-Halo constructs and stained with silicon rhodamine (SiR) or ATTO647 for 1 h at 37°C, 12 h post-electroporation. After washing with AIM-V medium, 4×10^3 CTLs were seeded on poly-L-ornithine and anti-CD3ε coated sapphire discs in flat specimen carriers for 10 min at 37°C and 5% CO_2, enabling the formation of an immunological synapse. Cells were vitrified in a high-pressure freezing system (EM PACT2, Leica) in AIM-V medium with 30% FCS and 10 mM HEPES.

For cryo-substitution, samples were transferred into the pre-cooled (−130°C) chamber of the AFS2 (Leica), where the temperature was increased gradually from −130 to −90°C over 2 h. Cryo-substitution was conducted at −90°C to −70°C for 20 h in anhydrous acetone and at −70°C to −60°C for 24 h with 0.3% uranyl acetate in acetone. Samples were infiltrated with increasing concentrations (30%, 60%, and 100%) of Lowicryl K11M/HM20 mixture for 1 h each, followed by 5 h of 100% Lowicryl infiltration. Samples were then UV polymerized at −60°C for 24 h and at 5°C for an additional 15 h. After polymerization, the carriers were removed, and ultrathin sections (100 nm) were cut using an EM UC7 ultramicrotome (Leica), mounted on carbon-coated 200-mesh copper grids (Plano).

Fluorescence analysis of EM sections was performed within 24 h post-sectioning to prevent loss of fluorescence signals. Grids were stained with DAPI (1:1000) for 3 min, washed, and sealed with silicone (Picodent Twinsil) for SIM imaging. After fluorescence imaging, grids were stained with uranyl acetate and lead citrate for electron microscopy, and captured on a Tecnai12 Biotwin transmission electron microscope (Thermo Fisher Scientific). Only CTLs with intact membranes, organelles, and nuclei were analyzed for correlation. DAPI images (405 nm) were used to align fluorescence with electron microscope images, allowing precise localization of fluorescent signals within cells. Image overlays were performed in Corel DRAW X6.

To analyze the isolated exosomes and organelles in the collected sucrose fractions, these fractions were diluted in D-PBS to a final sucrose concentration of 0.8 M, fixed with 2% PFA, and dropped on pioloform-coated copper grids. After fixation with 1% glutaraldehyde, samples were contrasted with uranyl acetate (Thery et al. 2006). Electron micrographs were acquired with the Tecnai 12 Biotwin electron microscope.

To compare the accumulation of organelles at the IS of WT and Munc13-4 KO CTLs, $CD8^+$ T cells were isolated as described above and cultured in Iscove's modified Dulbecco's medium (IMDM) supplemented with 10% fetal calf serum, 0.5% penicillin/streptomycin (Life Technologies) and 50 U/mL IL-2 at 37°C in a 5% CO_2 atmosphere. On day 3 anti-CD3/anti-CD28 activated CTLs (8×10^5) were harvested in fresh IMDM medium (1.49 mM Ca^{2+}) settled on poly-L-ornithine (0.1 mg/mL) and anti-CD3/anti-CD28 (10 μg/mL and 40 μg/mL, respectively) coated sapphire discs (1.4 mm diameter) in 4-well plates. The cells were incubated at 37°C and 5% CO_2 for 20 min and 1 h. Following incubation, cells on sapphire discs were transferred onto flat specimen carriers (Leica) and vitrified in IMDM medium containing 50% FCS using a high-pressure freezing system (EM PACT2, Leica). Freeze substitution and embedding in Epon 812 epoxy resin (Electron Microscopy Sciences) was performed as previously described (Liu et al. 2010). All samples were processed in an automatic freeze-substitution apparatus (AFS2, Leica). Briefly, samples were placed into the precooled (−130°C) freeze-substitution chamber of the AFS2 and the temperature was linearly increased from −130 to −90°C over 2 h. Cryo-substitution was performed in 2% osmium tetroxide in anhydrous acetone and 2% water. The temperature was increased linearly from −90°C to −70°C over 20 h, from −70°C to −50°C over 20 h, and from −50°C to −10°C over 5 h. After washing with anhydrous acetone, the cells were embedded in Epon-812 (30% Epon/acetone for 15 min at −10°C, 70% Epon/acetone for 1 h at −10°C and pure Epon for 1 h at 20 ± 2°C; Electron Microscopy Sciences). The temperature was increased linearly from 20 ± 2°C to 60°C for 4 h, and Epon was polymerized at 60°C for 24 h. Following polymerization, carriers and sapphire discs were removed from the resin block. Ultrathin (70 nm) sections were cut perpendicular to the former sapphire surface using an ultramicrotome (EM UC7; Leica), collected on Pioloform-coated copper grids, stained with uranyl acetate and lead citrate and analyzed with the Tecnai 12 Biotwin electron microscope (Thermo Fisher Scientific). The transmission electron microscopy (TEM) images were acquired using Olympus iTEM 5.0 image software (build1243). Only cells with intact and well-preserved membranes were included in the analysis. For the analysis of the cells that formed a prolonged synapse (1 h), the height of the cell was measured and divided by three. For the third of the cell in contact with the treated sapphire disc (straight edge of the cell), the cytoplasmic area without nucleus area and the number of organelles in this area were determined to calculate the organelle density. Only cells with mitochondria and at least

one of the organelles (SCG, MCG, MVB or early endosomes (EE)) present in this region of interest were analyzed. To calculate the organelle density of CTLs after 20 min contact, the cytoplasmic area of the complete section was determined. Organelle diameter was measured for all organelles present in the complete cell, both for cells with 20 min and 1 h contact.

2.13 | One-step Nanoscale Expansion (ONE) Microscopy

10X expansion of isolated exosomes was performed as follows. The samples were incubated at 4°C for 16 h with 0.3 mg/mL Acryloyl-X (A-20770, Thermo Fisher Scientific) in D-PBS pH 7.4. After incubation, coverslips were washed three times with D-PBS (5 min each) while preparing the gel monomer solution as previously described (Shaib et al. 2024). The solution was pipetted on parafilm and was covered with upside-down coverslips containing exosomes. The samples were incubated in a humidified chamber at room temperature for 16 h. Homogenization was performed by autoclaving for 60 min at 110°C in disruption buffer (5% Triton X-100 and 1% SDS in 100 mM Tris pH 8.0) followed by a 90-min incubation to cool the temperature to safe levels. Before autoclaving, the gels were washed first in 1 M NaCl and then at least four times in disruption buffer for a total time of at least 120 min. Gel expansion was performed by washing with double-distilled water (ddH_2O) for several hours, with at least five solution exchanges. The samples were labeled using a 20-fold molar excess of N-hydroxysuccinamide (NHS)-ester fluorescein (46409, Thermo Fisher Scientific) in $NaHCO_3$ buffer at pH 8.3 for 1 h before the washing procedure that induced the final expansion.

2.14 | Confocal Microscopy for Expansion Microscopy Acquisition

Images of expanded exosomes were acquired using a four-color STED Quadscan (Abberior, Göttingen, Germany) in confocal mode. A 100X/1.4NA objective (UPLSAPO 100XO, Olympus, Hamburg, Germany) was used with 485 nm (0.85 mW), 561 nm (2 mW), and 640 nm (12 mW) pulsed lasers. The pinhole size was set to 80 µm (1 AU), and acquisitions were carried out using detectors for GFP (498-520 nm, 30% laser power), Cy3 (40% laser power), and Cy5 (70% laser power). For the super-resolution radial fluctuations (SRRF) (Gustafsson et al. 2016; Laine et al. 2023) acquisition the parameters included a scan range of 10 µm × 10 µm (X × Y), a dwell time of 3.5 µs, and a pixel size of 98 nm. The maximum duty cycle was set to 82%, with line accumulation of 1, unidirectional scanning, and fast scan settings. A total of 1100 frames were acquired in 2 min and 19 s. The SRRF analysis was performed using the ONE platform (Shaib et al. 2024).

2.15 | Gel Electrophoresis of Proteins and Sample Preparation for Mass Spectrometry

Proteins were separated on NuPAGE and Bolt 4%–12% Bis-Tris gradient gels (Invitrogen) and stained with Coomassie G-250. Gel slices were washed with water and buffer A (50 mM NH_4HCO_3) and buffer B (50 mM NH_4HCO_3/50% acetonitrile). Disulfide bonds were reduced with 10 mM dithiothreitol at 56°C for 30 min, followed by carbamidomethylation with 5 mM iodoacetamide in the dark for 30 min at RT. Gel pieces were then vacuum dried, and in-gel digestion was performed using 20 µL of trypsin (10 ng/µL, Promega) overnight at 37°C. Extracted peptides were concentrated and resuspended in 0.1% formic acid for mass spectrometry analysis.

2.16 | Nano ESI-LC-MS2 Measurements

Tryptic peptides of CTL derived WT exosomes were analyzed by nanoflow LC-HR-MS/MS (Ultimate 3000 RSLC nano UHPLC system coupled to an LTQ Orbitrap Velos Pro, Thermo Scientific Bremen, Germany) according to Fecher-Trost et al. (2013) with modifications. Peptides were trapped on a C18 trap column and separated on a reversed-phase C18 capillary column (75 µm × 25 cm) with a flow rate of 200 nL/min for 120 min. The eluted peptides were ionized using a 2.2 kV electrospray emitter, and MS spectra were acquired in data-dependent mode, with the 10 most intense peptide ions fragmented by low-energy collision-induced dissociation (35% normalized collision energy). Tryptic peptides of CD63- and CD81- antibody enriched exosomes were concentrated and resuspended in 0.1% formic acid for nano nano-LC trapped ion mobility spectrometry (tims)-time-of-flight (TOF) MS analysis using a nanoflow-based UHPLC system (Bruker nanoElute, Bruker Daltonic, Bremen) connected to a timsTOF MS (timsTOF Pro 2, Bruker Daltonic, Bremen) with a nano-ESI source (nESI, CaptiveSpray). The instrument was calibrated according to the manufacturer´s recommendations. Extracted tryptic peptides were loaded on a PepMap Neo Trap Cartridge (300 µm x 5 mm, TF Scientific) and separated using a Thermo PepMap Neo column (500 mm x 75 µm, TF Scientific). Peptide elution was done using eluent A (water with formic acid (0.1%, v/v)) and eluent B (ACN with formic acid (0.1%, v/v)) for 120 min. The flow rate was set to 400nL/min and the column temperature was set to 50°C. Main parameters were: positive polarity; mass range 100–1700 m/z; 1/K0, 0.60–1.60 $Vs/cm^{2;}$ rolling average, on; TIMS, on; Parallel Accumulation Serial Fragmentation (PASEF) scan mode; General parameters were: moderate denoising mode; maximum intensity use for mass spectra peak detection; intensity threshold, absolute and 5000.0. TIMS mode parameters were: intraclass correlation (ICC), off; imeX mode, custom; 1/K0 start, 0.60–1.60 Vs/cm^2; ramp time, 100.0 ms; advanced parameters, on; lock accumulation to mobility range, on; accumulation time, 2.0 ms; target, 2.0 Mio; resolution, custom; spectra rate, n/a Hz; lock duty cycle to 100%, on. Captive Spray ion source parameters were: capillary, 1600 V; dry gas, 3.0 L/min;; nanoBooster, off; dry temperature, 180°C. General tune parameters were: deflection 1 delta, 70.0 V; funnel 1 radio frequency (RF), 300.0 Vpp; ion energy, 5.0 eV; collision energy, 10.0 eV; transfer time, 60.0 µs; high sensitivity detection, off; funnel 2 RF, 200.0 Vpp; multipole RF, 500.0 Vpp; low mass, 200.00 m/z; collision RF, 1500.0 Vpp; pre pulse storage, 12.0 µs; stepping, off. Parameters for receiving PASEF data were: number of PASEF MS/MS scans, 10; target intensity, 20,000; active exclusion, on; reconsider precursor, if, on; intensity threshold, 2500; charge range maximum, 5; release after, 0.40 min; current intensity/previous intensity, 4.00. PASEF-collision-induced dissociation parameters: advanced collision

energy settings, off; isolation mass start, 700.00 m/z; isolation width start, 2.00 m/z; 1/k0 Start, 0.60 Vs/cm^2; energy start, 20.00 eV; isolation mass end, 800.00 m/z; isolation width end, 3.00 m/z; 1/k0 end, 1.60 Vs/cm^2; energy end, 59.00 eV. PASEF-advanced parameters: MS repetitions, 1 x; summation width, 25 pts; mass width, 0.015 m/z; measuring time, 2.75 ms; cycle overlap, 4; maximum number of peaks, 3; 1/K0 width, 0.015 Vs/cm^2 and switching time was 1.65 ms.

2.17 | Raw LC-MS2 Data and Bioinformatic Analysis

Peptide identification of CTL derived WT exosomes analyzed with the Orbitrap Velos setup was performed using the MASCOT algorithm (Matrix Science) and TF Proteome Discoverer 1.4, searching the SwissProt database against mouse proteins (17040 mus musculus entries). The mass tolerance for precursor masses was set to 7 ppm, and for peptide fragment ions, it was set to 0.5 Da. Cysteine carbamidomethylation was set as a fixed modification, while variable modifications included deamidation of asparagine and glutamine, acetylation of lysine, and oxidation of methionine. Protein identification was confirmed when two unique peptides were matched per protein. Database search for CD63- and CD81-antibody-enriched exosomes analyzed with the timsTOF Pro 2 was done with PEAKS Studio software (version 10.6 build 20201221) with the following parameters: parent mass error tolerance, 15.0 ppm; fragment mass error tolerance, 0.1 Da; precursor mass search type, monoisotopic; enzyme, trypsin; maximum of three missed cleavage sites; semispecific digest mode; fixed modifications, carbamidomethylation (C), 57.02; variable modifications; oxidation (M), 15.99, acetylation (K, protein N-term), 42.01, and deamidation (NQ), 0.98; maximum of 5 variable post translational modification per peptide; database was taken from UniProt: mouse sp_tr_2024 including 21708 entries. The files belonging to a sample were merged, the precursor ions were corrected, and the charge filter was set to 2–8.

Due to possible variations between the experiments, we carried out a quantile-normalization of the expression values for all genes present on the respective data set using R (https://www.r-project.org). The quantile-normalized Log2 values were used for differential analysis with the limma framework. A linear model of the form ~ group with the two levels CD63 and CD81 (CD63 as reference) was fitted for every protein. Limma's empirical Bayes procedure moderated the standard errors across proteins, improving statistical power in small-sample settings. For each protein, the model returned a Log_2 fold change ($\log_2$FC) comparing CD81 versus CD63, a moderated t-statistic, a raw p-value, and a Benjamini–Hochberg false discovery rate (FDR / adjusted p value).

Proteins, that were identified as significantly enriched in CD63 or CD81 fractions were further analyzed by GO term enrichment analysis (for biological processes, molecular function and cellular component) with the free software ShinyGO v0.741 with 0.05 FDR cutoff (http://bioinformatics.sdstate.edu/go/)(Xejin G, Jianil Q, Spors E et al. South Dakota State University (SDSU)). Heat maps were created with the program Morpheus (http://software.broadinstitute.org/morpheus) using the Log2 values of the normalized abundance of proteins.

2.18 | Killing Assay and Flow Cytometry Analysis of Exosome Cytotoxicity

To assess the cytotoxic effects of exosomes isolated from CD8$^+$ T lymphocytes, P815 cells were plated at 5×10^4 cells per well and treated with 10 µg of exosomes for 12 and 24 h at 37°C and 5% CO_2. Positive controls included lysis of P815 cells with H_2O_2 or DMSO. After treatment, cells were stained with caspase 3 and propidium iodide (PI) using the Vybrant FLICA Caspase Apoptosis Assay Kits (V35118, Thermo Fisher Scientific) for flow cytometry following the manufacturer's instructions. Gates were set to include both live and dead cells. Data acquisition was performed using a BD FACSAria III analyzer, and analysis was conducted with FlowJo v10.0.7 software.

2.19 | Statistics

Data were tested for significance with SigmaPlot (Systat Software Inc.), IgorPro 6.37 (Wavemetrics) or R (https://www.r-project.org) using Student T test, Mann–Whitney-Test, and Kruskall–Wallis-Test: $^*p < 0.05$, $^{**}p < 0.01$, $^{***}p < 0.001$. The box plots show the median, the 25 and 75 percentile and the 10 and 90 percentiles as whiskers.

3 | RESULTS

3.1 | CD63 co-localizes With Granzyme B Positive Organelles in Mouse CTLs

Tetraspanins, particularly CD63 and CD81, are well-established as markers for exosomes and multivesicular bodies (MVBs) in a variety of cell types (van Niel et al. 2018; Welsh et al. 2024). However, in cytotoxic T lymphocytes (CTLs), tetraspanins exhibit reduced specificity and are also found on cytotoxic granules (CGs) (Metzelaar et al. 1991; Peters et al. 1991). To investigate the expression and spatial distribution of CD63 and CD81 in murine CTLs, we co-transfected day 4 CTLs with CD63-pHuji and CD81-SEP constructs. Following transfection, we plated the cells on anti-CD3ε coated coverslips to facilitate IS formation and stained them with anti-GzmB antibody for super-resolution structured illumination microscopy (SIM) (Figure 1a). SIM imaging revealed robust co-localization of CD63 with GzmB, whereas the degree of co-localization between CD81 and GzmB was comparatively low, as quantified by Manders' overlap and the Pearson's correlation coefficient (Figure 1b). The intermediate co-localization coefficients for CD81 and CD63 indicated that both markers can localize to distinct subcellular structures. To further validate the specificity of CD63 and CD81 as markers for ILV-bearing organelles, we conducted correlative light-electron microscopy (CLEM) on day 4 GzmB-mTFP KI CTLs. These cells were electroporated with either CD63-Halo or CD81-Halo constructs and stained with SiR-647 after 12 h expression time in culture. The cells underwent high-pressure freezing and were prepared for post-embedding CLEM. In alignment with the high co-localization of CD63 with GzmB observed in SIM (Figure 1b), the CLEM analysis revealed that CD63 localized not only to MVBs but also to GzmB$^+$ organelles, including both SCGs and MCGs (Figure 1c,d). GzmB was associated with electron-dense regions within the organelles. CD81 exhibited a more

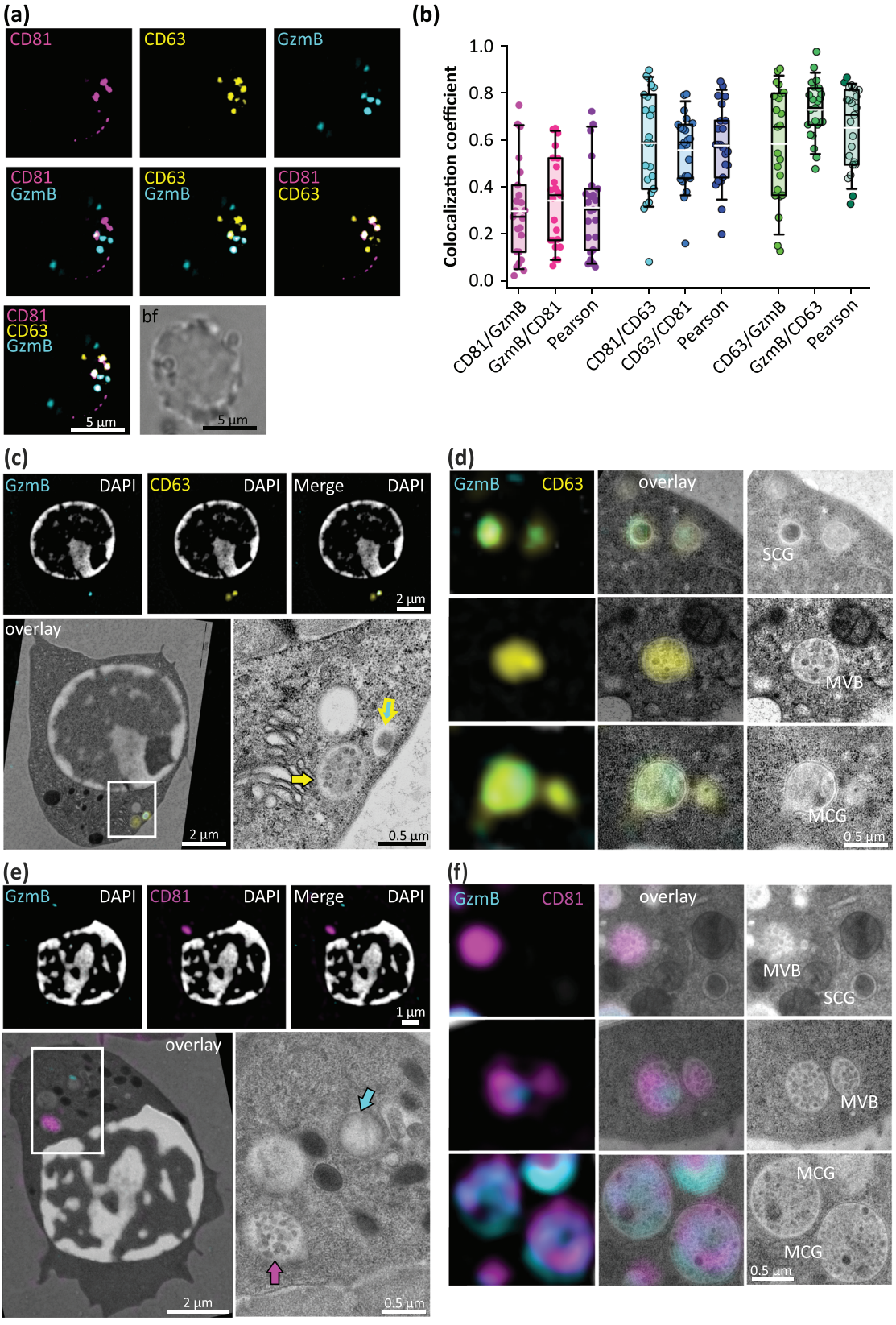

FIGURE 1 | CD81 is a more specific exosome marker in murine CTLs than CD63. (a) Representative single-plane structured illumination microscopy (SIM) images of primary murine CTLs electroporated with CD81-SEP (magenta) and CD63-pHuji (yellow) and immune-stained with an anti-granzyme B (GzmB) antibody coupled to Alexa 647 (cyan). Cells were seeded on anti-CD3ε coated coverslips for 10 min prior to fixation to induce immunological synapse (IS) formation. (b) Mander's and Pearson's co-localization coefficients between CD81 and GzmB, CD81 and CD63, and GzmB and CD63. N_{mice} = 3 independent experiments, n_{cells} = 20. The box plot shows the median and the 25 and 75 percentiles, while the whiskers correspond to the 10 and 90 percentiles. (c) Representative correlative light electron microscopy (CLEM) image of GzmB-mTFP knock in CTLs electroporated with CD63-

restricted expression profile, being exclusively associated with ILV-containing MVBs and MCGs. We did not detect a CD81 signal in SCGs, reinforcing its specificity for ILV-bearing organelles in murine CTLs (Figure 1e,f). Taken together, these results suggest that CD63 serves as a ubiquitous marker for MVBs and cytotoxic organelles, including both SCGs and MCGs, while CD81 is a more specific marker for ILV-containing organelles in murine CTLs.

3.2 | CD63-positive Exosomes Are Released From MCGs

Since we showed that CD63 is a more general organelle marker, localized to SCGs, MCGs, and MVBs, we utilized this property to compare the release kinetics and to quantify the number of fusion events of these organelle types at the IS. We co-transfected day 4 WT CTLs with CD63-SEP and GzmB-pHuji, as described by Alawar et al. (2024) and analyzed them after 12 h in culture. We seeded the cells on anti-CD3ε coated glass coverslips to induce IS formation and superfused the cells with calcium containing solution at RT to increase granule fusion events, which we measured using TIRF microscopy (Figure 2a,c, Supp. Movie 1 and 2). For the tetraspanins, the pH sensitive fluorescent proteins are cloned into the first extracellular loop and thus report on the luminal versus extracellular pH on fusion with the plasma membrane. Individual fusion events were identified by a fast increase in fluorescence for CD63-SEP and GzmB-pHuji due to the deprotonation of the granule lumen, followed by the dispersion of the label (Figure 2b,d). We analyzed the fluorescent signal kinetics (Figure 2b,d) and determined the decay time, defined as the time required for the fluorescence signal to decrease to 63% of its peak intensity, for each fusion event in both channels (Figure 2e,f). The decay time of fluorescence intensity allowed us to determine whether CD63-SEP was localized exclusively to the organelle membrane or also to the released exosomes (Estl et al. 2020; Verweij et al. 2018). A fast fluorescence decay time of less than 2 s indicates that CD63-SEP is localized to the organelle membrane as it can quickly diffuse in the plasma membrane upon exocytosis. In contrast, if the decay time is longer than 2 s, it is likely that CD63-SEP is also contained in exosomes. These get trapped between the plasma membrane and the glass coverslip and only slowly spread away from the release site (Verweij et al. 2018). For GzmB-pHuji a long decay time denotes the release of SMAPs in which GzmB aggregates and therefore does not move away from the release site (Balint et al. 2020; Chang et al. 2022). A decay time of less than 2 s represents the secretion of diffusible GzmB-pHuji, with rapid cargo dispersal (Estl et al. 2020). This was the case for approximately 70% of the GzmB$^+$ events. In contrary a fast diffusion of CD63 is only observed in about 26% of the events. A large majority of the CD63$^+$ events exhibited a longer decay times (>2 s), indicating the prolonged presence of secreted CD63$^+$ exosomes on the glass coverslip (Figure 2d,f). Fusion events with prolonged decay times in both channels, indicate the co-release of CD63$^+$ exosomes and GzmB$^+$ SMAPs localized in MCGs (Figure 2c,d,f) (Chang et al. 2022). TIRF microscopy analysis of GzmB-mTFP KI CTLs expressing CD63-pHuji on supported lipid bilayer (SLB) under similar stimulation conditions (Figure S1) revealed comparable results with a slightly increased percentage of fast decaying events. Additionally, the percentage of fusion events with very long decay times (>50 s) was nearly abolished (Figure S1e) indicating higher mobility of secreted exosomes on SLBs than on glass. To better categorize the fused organelles, the decay times of the two fluorescent markers were plotted against each other for all CD63$^+$ fusion events (Figure 2g). CD63$^+$ GzmB$^-$ events, were indicative for MVB fusion especially since the decay time was always longer corresponding to exosome release. CD63$^+$ GzmB$^+$ fusion events with CD63-pHuji decay times of less than 2 s (below the gray stippled line) likely corresponded to SCGs fusion events. CD63$^+$ GzmB$^+$ fusion events with extended decay times, resulting from the release and the accumulation of exosomes and SMAPs on glass coverslips after secretion, reflect the population of MCGs.

Overall, TIRF microscopy analysis revealed that 28.7 ± 2.8% of transfected cells exhibited fusion events with an average of 2.5 ± 0.8 events per transfected cell. 69.84% of these events were MCG events and 26.20% were SCG events (Figure 2h,i). To examine the localization of CD63$^+$ cytotoxic granules fusion at the IS, cells were co-transfected with CD63-pHuji and Lifeact-GFP to highlight the p-SMAC region. CD63$^+$ organelles fused predominantly within the c-SMAC (Figure S2). In conclusion, these results indicate distinct fusion kinetics and cargo release patterns, with SCGs showing rapid CD63 membrane diffusion and soluble GzmB release, while MCGs exhibit more prolonged co-release of exosome-associated CD63 and the SMAP component GzmB.

3.3 | Exosomes Released From MCGs Exhibit a Heterogeneous Tetraspanin Expression

Exosomes secreted by different cell types display distinct markers and contents, contributing to various biological functions (Welsh et al. 2024). Beyond intercellular variability, there might be

Halo, stained with silicon rhodamin (SiR) 647 (yellow) and DAPI (white). Shown are SIM images (top row) and the overlay with the corresponding electron micrograph (lower panel, left). The white rectangle marks the magnified region with identified organelles (lower panel, right). Arrows with the corresponding color scheme as shown in the SIM images (upper row) mark CD63$^+$ and a CD63$^+$ GzmB$^+$ compartments. (d) Representative CD63$^+$ (yellow) and CD63$^+$ GzmB$^+$ (yellow and cyan) double positive organelles, cropped from three mouse CTL CLEM images as displayed in (*c*). Shown from left to right are the corresponding SIM, CLEM, and TEM images. (e). Representative CLEM image of GzmB-mTFP (cyan) knock in mouse CTL electroporated with CD81-Halo stained with ATTO647 (magenta) and DAPI (white). Shown are SIM images (top row) and the overlay with the corresponding electron micrograph (lower panel, left). In the magnified electron micrograph (lower panel, right) cyan and magenta arrows denote GzmB$^+$ and CD81$^+$ compartments, respectively. (f) Representative CD81$^+$ (magenta) and CD81$^+$GzmB$^+$ (magenta, cyan) double positive organelles, cropped from three mouse CTL CLEM images as shown in (*e*). Shown from left to right are the corresponding SIM, CLEM, and TEM images. *N* = 2 independent experiments, n_{CD63} = 13 and n_{CD81} = 15. SCG, single core granule; MCG, multi core granule; MVB, multivesicular body; SMAPs, supramolecular attack particles; SEP, super ecliptic pHluorin.

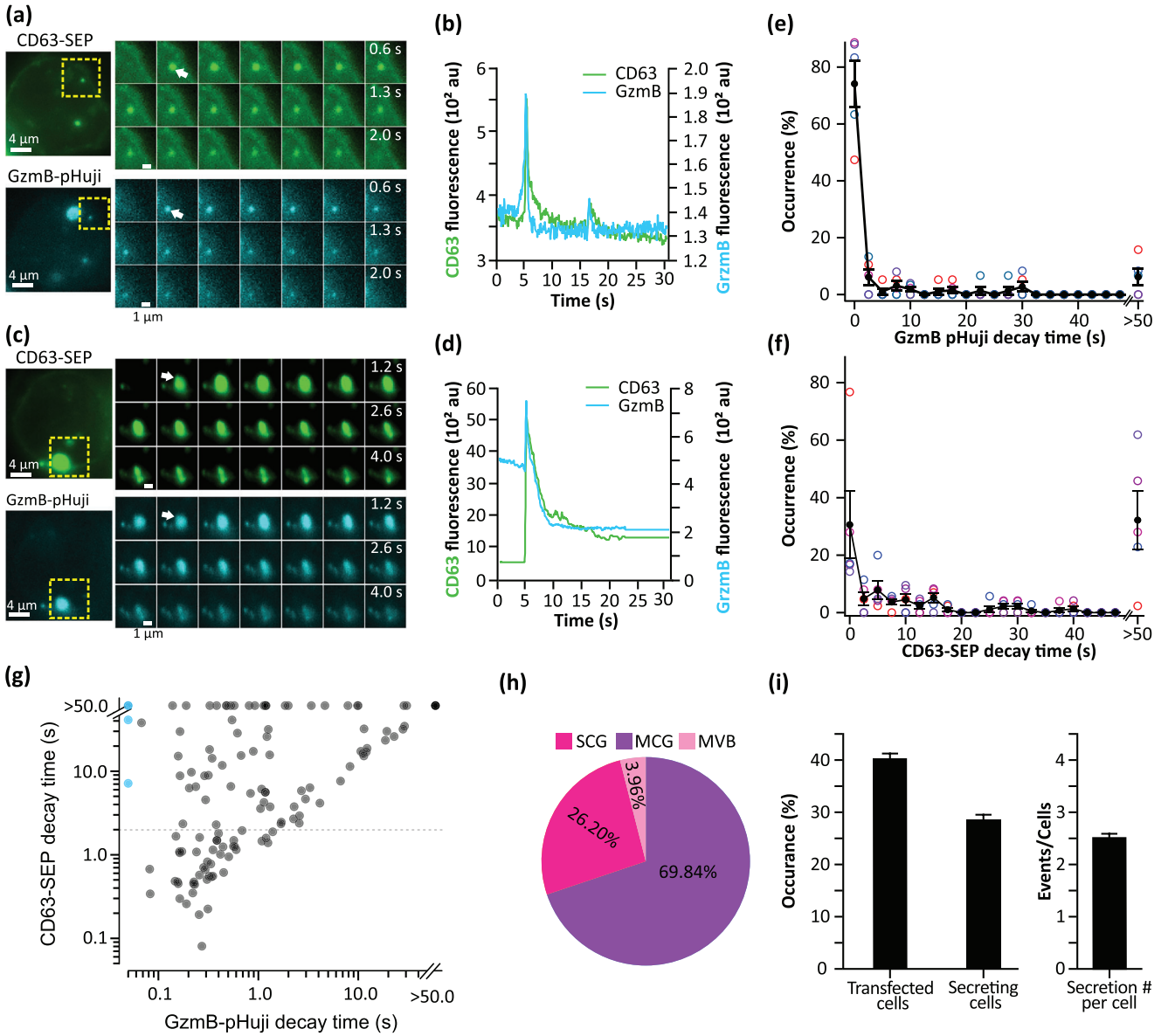

FIGURE 2 | Visualization of exosomes and SMAPs release from MCGs at the immune synapse. Total internal reflection fluorescent (TIRF) microscopy snapshots of WT CTLs electroporated with CD63-SEP (green) and GzmB-pHuji (cyan) and settled on anti-CD3ε coated coverslips. (a) Representative WT CTL showing a fast fusion event (white arrow) corresponding to a typical SCG fusion. (b) The corresponding fusion profile of the event detected in (*a*), showing a sharp increase in the fluorescence intensity of CD63 and GzmB accompanied by a rapid decrease in fluorescence intensity. (c) Representative MCG fusion event (white arrow) showing a very long signal duration with visible exosomes and SMAPs after secretion labeled with CD63 and GzmB respectively. (d) The corresponding fusion profile of the MCG fusion event shown in (*c*), displaying a long signal duration of CD63 and GzmB fluorescence. The decay times of all analyzed GzmB-pHuji (e) and CD63-SEP (f) events. Open circles in blue, red, and green reflect independent experiments. $N = 3$, data represented as mean ± SEM. (g) Correlation plot of the decay times of CD63-SEP as a function of the decay time of GzmB-pHuji. Decay time above 2 s (stippled gray line) correspond to exosome release. (h) The percentage of SCG, MCG, and MVB events analyzed from the total experiments. (i) Shown is the percentage of CD63-SEP and GzmB-pHuji co-transfected cells, the percentage of secreting cells, and the number of events per cell. $N_{mice} = 5$, $n_{cells} = 59$, $n_{events} = 149$. Images were recorded at 10 Hz. SCG, single core granule; MCG, multi core granule; SMAPs, supramolecular attack particles; GzmB, Granzyme B; SEP, super-ecliptic pHluorin.

an intracellular heterogeneity of ILVs within MCGs and MVBs in murine CTLs leading to release of distinct exosomes. A particularly intriguing finding is that only 3.96% of the events at the IS were attributed to MVBs fusion as they lack a GzmB signal (Figure 2h). This suggests that while MVBs may mediate more random or unpolarized, IS-independent exosome secretion, MCGs are the major contributors to polarized exosome release at the IS (Figure S2). The lower co-localization of CD81 and CD63 on individual cell structures, as observed by SIM on anti-CD3ε stimulated CTLs (Figure 1a,b), indicates high heterogeneity in tetraspanin localization. To further investigate the expression of tetraspanins in MCGs, we analyzed the fusion dynamics of $CD81^+$ and $CD63^+$ MCGs using TIRF microscopy. WT CTLs were co-transfected with CD63-pHuji and CD81-SEP, added on anti-CD3ε coated glass coverslips and stimulated with high calcium containing solution as described previously (Figure 2).

The analysis of fusion events revealed a highly heterogeneous profile that could be categorized into distinct patterns. In each of the representative fusion events, a rapid increase in fluorescence intensity for CD63 and CD81 was observed within milliseconds, indicating the fusion event, but they exhibited distinct decay times. As described for CD63-pHuji, a fast decay time in the CD81-SEP signal indicates that it is primarily localized to the organelle membrane and diffuses quickly in the plasma membrane upon exocytosis. Conversely, a slow fluorescence decay indicates the release of CD81-pHuji labeled exosomes. Therefore, a fast decay for both markers suggests that both are localized to the organelle membrane and would correspond to SCG exocytosis that do not contain exosomes. As expected this occurs rarely since SCG do not contain CD81 (8.6% of the events) as shown in figure 1f. A slow decay for both markers suggests that MCGs fused with the plasma membrane and released CD81- and CD63-positive exosomes (see Figure 3a and b, and Movie S3 and S4). This is the case for a large majority of the events (71.4%, Figure 3g). Furthermore, a vast majority of these events (>70%) exhibited a longer decay time for CD63 than for CD81 (Figure 3e–g, Movie S4). A long decay time (>2 s) for CD63 in comparison to CD81 (Figure 3c,d, and Movie S5) indicates that the fusing MCG contained primarily $CD63^+$ exosomes, prolonging its post-fusion signal (Verweij et al. 2018). This occurred in 17.1% of events. The converse, CD63 showing a short decay time (<2 s) and CD81 showing a long decay time (>2 s) almost never occurred (>3% of the events, Figure 3g lower right quadrant). Overall, these findings indicate that CD81 is more predominantly associated with the organelle membrane, whereas CD63 is highly enriched on the exosome membrane within MCGs.

3.4 | CD81 is a Specific Marker for MVB and MCG Membranes

To determine whether the membranes of the characterized organelles exhibit differences in their tetraspanins content, as shown by the distinct fusion dynamics of $CD81^+$ and $CD63^+$ organelles in TIRF microscopy, we isolated MVBs, MCGs and SCGs from CTLs for immune analysis. We assessed day 5 activated CTLs for viability, activation state, and subtype distribution by flow cytometry (Figure S3a–c). We broke the cells open using nitrogen cavitation, and subjected the resulting homogenate to discontinuous sucrose density gradient ultracentrifugation (Figure 4a). The protocol, adapted from previous studies (Chang et al. 2022; Schirra et al. 2023), enabled the isolation of MVBs along with MCGs and SCGs within the same sucrose gradient. We characterized eight sucrose fractions (1-8) by Western blotting and we analyzed fractions 4, 6, and 8 by TEM (Figure 4b,c). Western blot analysis revealed the presence of GzmB in sucrose fractions 6 and 8, corresponding to MCGs and SCGs, respectively (Figure 4b). TEM analysis confirmed the presence of intact organelles in these fractions (Figure 4c). The high concentration of the v-SNARE VAMP7 identified the MVBs in fraction 4, since this SNARE protein has been shown to mediate MVB fusion with the plasma membrane (Liu et al. 2023). In contrast fractions 6 and 8 exhibited only low amount of VAMP7, consistent with the previous findings that VAMP2 is the v-SNARE for cytotoxic granule secretion in mouse CTLs (Chang et al. 2022). The absence of GzmB and EEA1 in fraction 4 further supports the specificity of the MVB isolation procedure (Figure 4b,c). Immunofluorescence analysis was performed with isolated organelles from fraction 4, 6 and 8, which were concentrated on gelatin-coated coverslips. In order to ascertain whether these organelles exhibit differential tetraspanin content within the membrane, surface staining for CD81, CD63, and Lysobisphosphatidic acid (LBPA), a marker of MVBs, was conducted without permeabilization. We acquired the images using SIM, which we segmented using Cellpose 2.0 (Pachitariu and Stringer 2022) to perform an object-based co-localization analysis (Figure 4d,e). To ensure accuracy of the analysis, only organelles larger than 200 nm in diameter (fraction 8) or 350 nm (fractions 4 and 6) that co-localized with LBPA were included, thus excluding exosomes or fragmented membranes resulting from disrupted organelles. The results revealed significant differences in tetraspanin content among the organelles. MVBs and MCGs exhibited significantly higher levels of CD81 on their membranes compared to SCGs, with 79.1 ± 2.1% of MVBs and 73.2 ± 2.1% of MCGs being $CD81^+$, while only 31.9 ± 8.8% of SCGs were positive for CD81. In contrast, SCG membranes were enriched in CD63 relative to MVBs and MCGs, with 64.5 ± 9.5% of SCGs being $CD63^+$, compared to just 14.4 ± 2.1% of MVBs and 15.5 ± 1.6% of MCGs (Figure 4d,e). Pie charts summarizing the overall distribution of all $CD63^+$ and/or $CD81^+$ events across MVBs, MCGs, and SCGs are shown in Figure 4f.

These results indicate that CD81 is more abundant on the membranes of MVBs and MCGs than on SCGs membranes. Furthermore, the experiment confirms the low co-localization of CD63 and CD81 on MVBs and MCGs membrane.

3.5 | Isolated T-cell Derived Exosomes Show Two Subpopulations Based on Size

To determine whether there is a heterogeneity of exosomes from MVBs and MCGs in function and morphology, we activated 10×10^6 CTLs for 5 days using anti-CD3/anti-CD28 coated beads and expanded them in exosome-depleted FCS media. We subsequently isolated the small EVs from the supernatant of $600–800 \times 10^6$ CTLs via differential ultracentrifugation. They were pelleted at 100,000 × *g*, and an optimized sucrose density gradient allowed us to further purify and enrich the exosome fractions. The density of exosomes was expected to be between 1.15 and 1.19 g/cm^3 (Thery et al. 2006), therefore they should be mainly enriched in a sucrose density fraction of 1.2 M. To isolate potentially distinct sized exosome present in the supernatant of expanded CTL cultures, we included additional sucrose fractions of 1.1 and 1.3 M (Figure 5a). TEM analysis revealed the presence of particles in fractions 1.1, 1.2, and 1.3 M. Notably, we detected two distinct size populations in these fractions: one ranging from 30–80 nm (53%) and another from 80–150 nm (39%) (Figure 5b). The different sucrose fractions were then analyzed by Western blotting for exosome markers. Western blot analysis confirmed the presence of exosomes by the detection of ALIX and TSG101 in fractions 1.1, 1.2, and 1.3 M (Figure 5c). In order to avoid the exclusion of minor subpopulations and to maximize the yield of exosomes for further studies, such as mass spectrometry (MS), immune analysis, or physiological investigations, we pooled exosomes isolated from fractions 1.1, 1.2, and 1.3 M. The pooling strategy enabled successful detection of the tetraspanin CD81 (Figure 5d). We validated the presence and purity of the isolated exosomes by MS analysis. A total of 824 proteins were

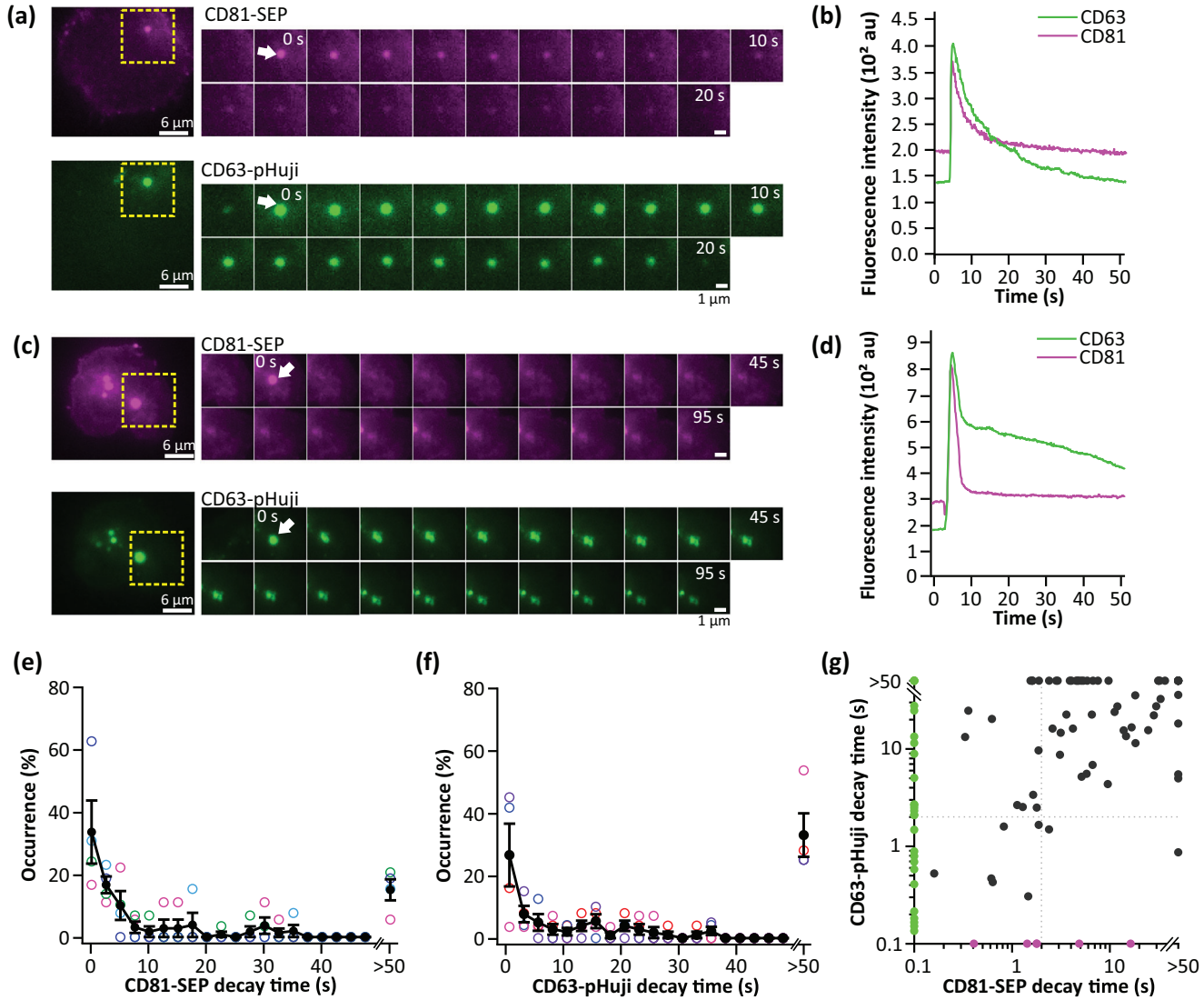

FIGURE 3 | Exosomes containing organelles show heterogeneity in the expression of tetraspanins. Total internal reflection fluorescence (TIRF) microscopy snapshots of WT CTLs electroporated with CD81-SEP (magenta) and CD63-pHuji (green) and settled on anti-CD3ε coated coverslips. (a) Representative CTL showing an MCG fusion event (white arrow). (b) The corresponding fusion profile of the event detected in (*a*), showing a similar fusion profile for CD81-SEP and CD63-pHuji. (c) Representative CD81-SEP and CD63-pHuji labeled MCG fusion event (white arrow) showing a long signal duration of CD63-pHuji with visible CD63-positive exosomes after secretion and short CD81-SEP signal duration with no visible CD81 labeled exosomes post secretion. (d) The corresponding fusion profile of the MCG fusion event shown in *(c)*, displaying a longer signal duration of CD63-pHuji in comparison to CD81-SEP. Images were recorded at 10 Hz. The decay time of CD81-SEP (e) and CD63-pHuji (f) of all analyzed events. Open circles in blue, red and green reflect independent experiments. $N = 3$, data represented as mean ± SEM. (g) Correlation plot of the decay times of CD63-pHuji as a function of the decay time of CD81-SEP. Shown in magenta are the decay times of CD81-SEP positive fusion events without detection of CD63-pHuji. Shown in green are the decay times of CD63-pHuji positive fusion events without detection of CD81-SEP. Shown in grey are the decay times of the CD81-SEP and CD63-pHuji positive fusion events. $N_{mice} = 5$, $n_{cells} = 54$, $n_{events} = 103$. SCG, single core granule; MCG, multi core granule; SEP, super-ecliptic pHluorin.

identified from WT exosome samples, based on a stringent 1% false discovery rate (FDR) and a minimum of two unique peptides per protein (Table S2). The identified proteins were compared to the Top 100 proteins listed in the Exocarta database (http://exocarta.org/sEV_top100 (Ghosh et al. 2025)). Among these, 79 proteins of the CTL-derived exosomes were included in the Top 100 list (Figure 5e). Importantly, calnexin, a marker of endoplasmic reticulum contamination, was absent, indicating the high efficiency of the isolation protocol in yielding pure exosomes with minimal contamination. We found only 3 peptides of GzmB, no peptides of thrombospondin 1 or 4 (TSP-1 or TSP-4), and no perforin (Prf1), indicating very little contamination by SMAPs. This was confirmed by an anti-GzmB immunostaining of the isolated exosomes (Figure S4). None of the typical corona proteins (APOH, CLUS, FIBA, FIBG, HPT) were present confirming our TEM analysis (Toth et al. 2021). Further analysis of the subcellular localization of the identified proteins revealed that 63.83% of the proteins were known extracellular vesicle markers, while only 0.12% and 0.24% were markers of the Golgi and ER, respectively (Figure 5f).

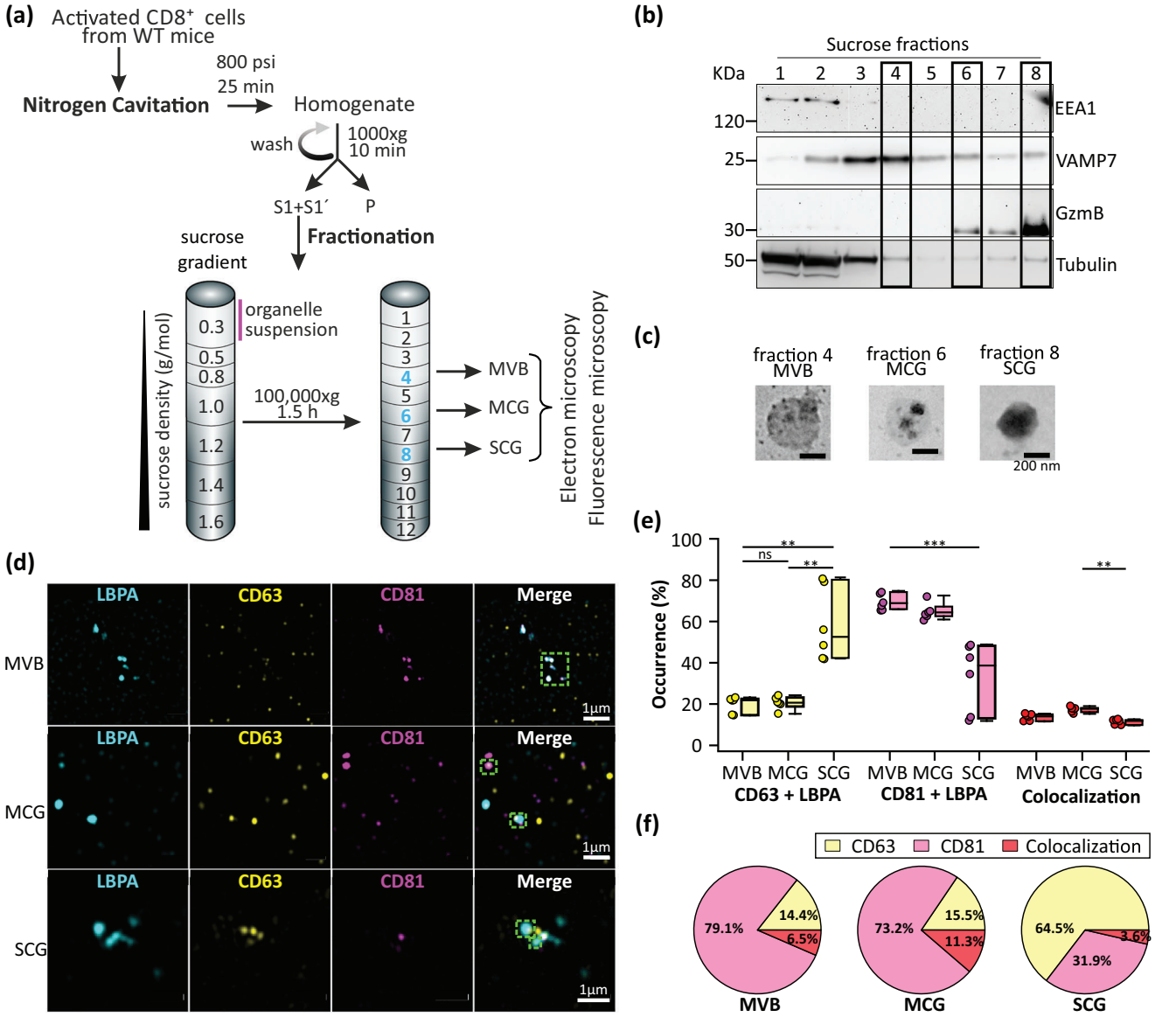

FIGURE 4 | The tetraspanin CD81 is a more specific MVB and MCG marker in murine CTLs than CD63. (a) Schematic representation of the subcellular fractionation of MVBs, MCGs, and SCGs from murine CTLs. (b) Representative Western blot of the different sucrose fractions (1–8) probed against early endosome marker (EEA1), SNARE protein (VAMP7), cytotoxic granule marker (GzmB) and cytoskeleton marker (tubulin). (c) Representative transmission electron microscopy (TEM) images of organelles present in sucrose fractions 4, 6, and 8 corresponding to multivesicular body (MVB), multi core granule (MCG), single core granule (SCG), from three independent experiments ($N_{gradients} = 3$). (d) Representative organelles corresponding to MVBs (top row), MCGs (middle row), and SCGs (bottom row). The organelles were isolated from the corresponding sucrose fractions of WT CTLs as shown in (*c*), centrifuged on gelatin-coated coverslips, fixed, and stained with anti-LBPA (cyan), anti-CD63 (yellow), and anti-CD81 (magenta) antibodies. Images were acquired with structured illumination microscopy (SIM). Shown are the images of the individual channels and the merge of all three channels images. (e) Object-based co-localization analysis of all three proteins displayed as scatter dot plots with the values superimposed with a box plot comprising the median (black line). (f) Pie chart representing the percentage of tetraspanins in each of the isolated organelles. $N_{gradients} = 3$, from three independent experiments, organelles analyzed: $n_{SCG} = 7620$, $n_{MCG} = 11245$, $n_{MVB} = 11720$. SCG, single core granule; MCG, multi core granule; MVB, multivesicular body; LBPA, lysobisphosphatidic acid; ns, not significant. Data represented as mean ± SEM, data significance was analyzed by the Kruskal–Wallis test, $^{**}p < 0.01$, $^{***}p < 0.001$.

Additionally, we categorized the identified proteins into several functional categories (Table S3). Proteins involved in vesicle formation, transport, and fusion were well-represented. High levels of CD82 and TSG101, both essential for exosome biogenesis, were detected. Proteins linked to immune signaling and modulation, such as MHC class I molecules and other immune-related proteins, were present, suggesting a potential role of CTL-derived exosomes in immune surveillance or antigen presentation (Morelli et al. 2004; Raposo and Stoorvogel 2013). The exosome cargo also contained key signaling molecules, implicating their potential function in cell-to-cell communication. Proteins associated with cellular stress, such as HSP70, were abundant, supporting the hypothesis that heat shock proteins may facilitate antigen loading onto exosomes, a process relevant

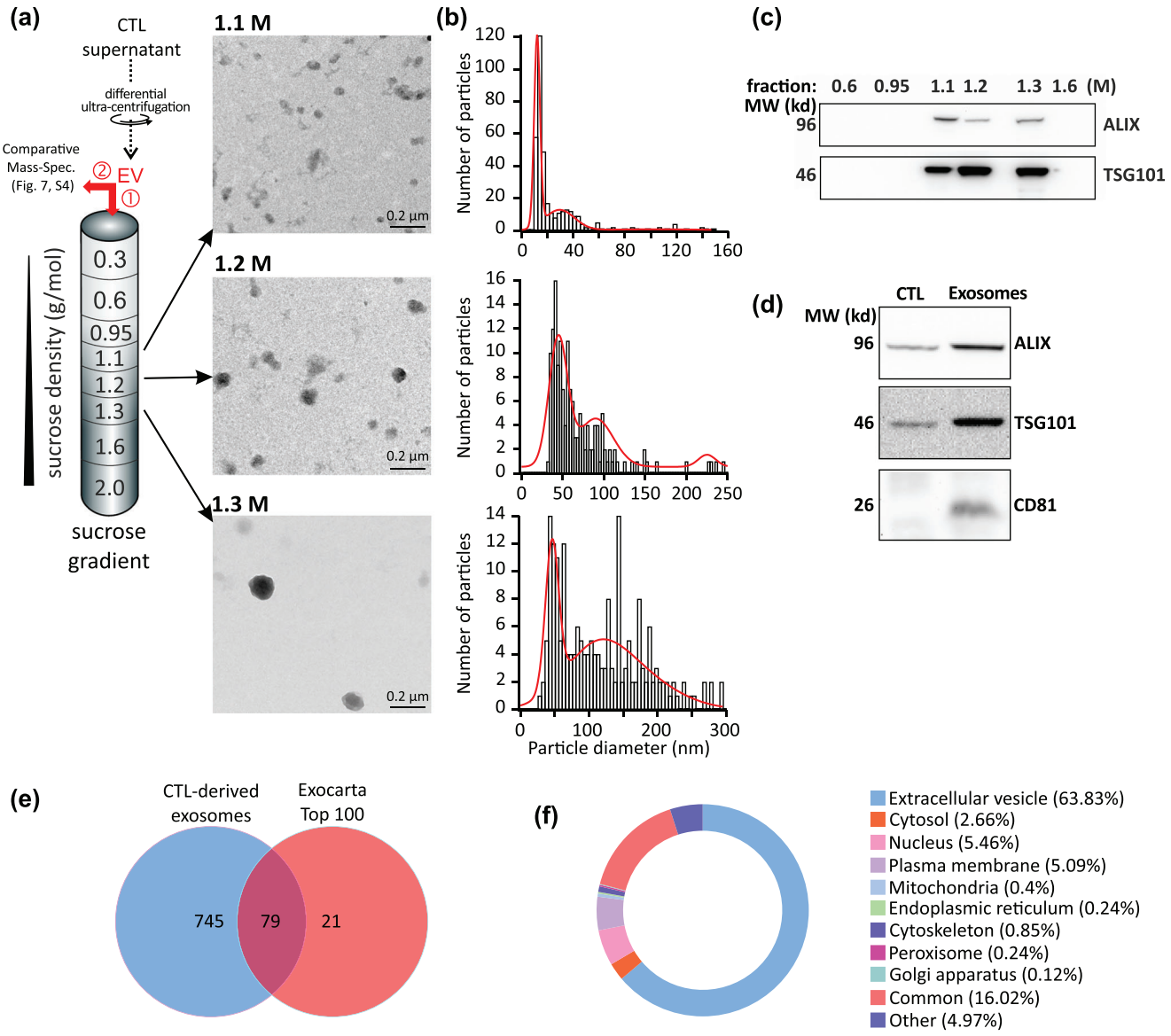

FIGURE 5 | Characterization of exosomes isolated from primary murine CTLs. (a) Scheme for isolation of highly pure exosome from EV sample with a density sucrose gradient (①)for analysis using transmission electron micrographs of sucrose fractions 1.1 M, 1.2 M, and 1.3 M with the diameter analysis of each fraction shown in (*b*). 10 µL of each sucrose fraction were PFA fixed, dropped on a copper grid and prepared for electron microscopy. EVs samples are also used for a comparative mass spectrometry analysis (②) described below. (b). Fit of particle diameter was done with double and triple gaussian. (c) Western blot for sucrose fractions 0.6–1.6 M (10 µg protein/lane) probed against exosome markers ALIX and TSG101. (d) Western blot for cytotoxic T lymphocyte (CTL) lysate and exosomes pooled from fractions 1.1 M, 1.2 M, and 1.3 M probed against the exosome markers ALIX, TSG101, and CD81. (e) Venn diagram displaying the number and overlap of proteins identified in mass spectrometry analysis from WT murine CTLs-derived exosomes isolated in this study with those in the Exocarta Top 100 exosome proteins. (f) Pie chart showing the subcellular location of the total identified proteins predicted by Scaffold software.

for immune modulation and cytotoxicity in CTLs (Reddy et al. 2018). Moreover, metabolic enzymes, including GAPDH, were also identified, suggesting that exosomes may be involved in metabolic regulation or serve as carriers of metabolic information for intercellular communication. Finally, we found proteins involved in the apoptotic pathway including STAT1, Caspase3, and BAX suggesting a supporting role in target cell killing (Bedoui et al. 2020). In summary, the mass spectrometry data, together with the results from Western blotting and TEM, not only confirm the purity of the exosome preparation but also highlight the functional and morphological diversity of exosomes secreted by CTLs.

3.6 | The Tetraspanins CD63 and CD81 Localize on Different Exosomal Subpopulations

To investigate tetraspanin expression on murine T-cell derived exosomes, we pooled the exosomes isolated from sucrose fractions 1.1, 1.2, and 1.3 M and pelleted them on 2% gelatin-coated coverslips by ultracentrifugation at 20,000 × *g* for 4 h. After pelleting, we immediately fixed, permeabilized, and stained the exosomes with antibodies against CD81 and CD63. We imaged the samples with SIM (Figure 6a) and performed a colocalisation analysis. Surprisingly, we observed a very low degree of co-

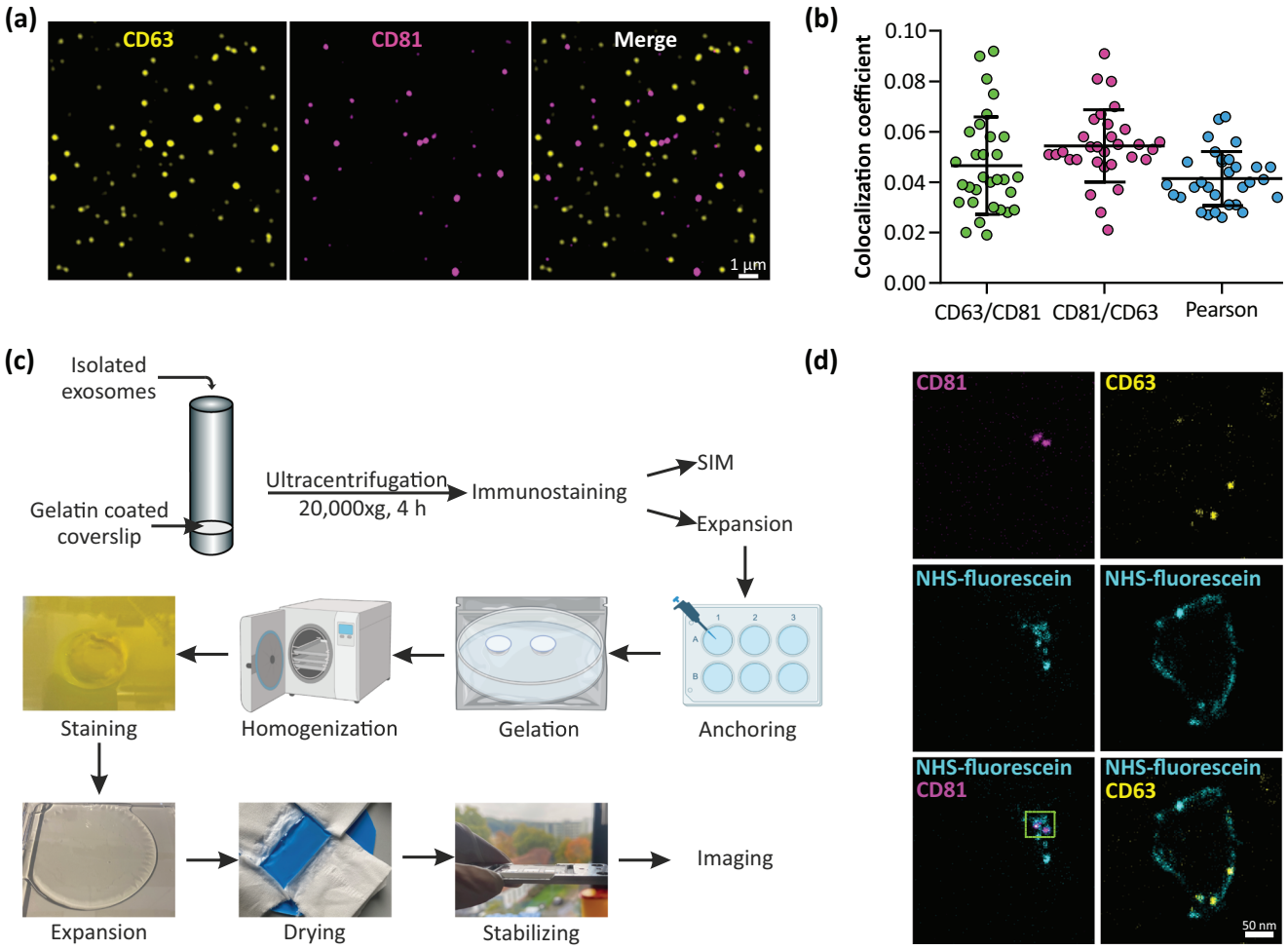

FIGURE 6 | Exosomes derived from murine CTLs are divided based on their tetraspanins surface marker into two subpopulations, CD63- and CD81-positive exosomes. (a) Representative structured illumination microscopy (SIM) images of exosomes isolated from WT CTLs, centrifuged on gelatin-coated coverslips, fixed, and stained with anti-CD63 (yellow) and anti-CD81 (magenta) antibodies. Shown are the images of the individual channels and the merge image of the two channels. (b) Mander's and Pearson's co-localization coefficients between CD81 and CD63. Data represented as mean ± SEM, $N = 3$ independent experiments. (c) Schematic representation of the 10X expansion procedure (One-step nanoscale expansion (ONE)-microscopy) for isolated exosomes. Exosomes isolated from WT CTLs were pelleted on gelatin-coated coverslips, fixed, and stained against the tetraspanins CD81 (magenta) and CD63 (yellow). Stained exosomes were then subjected to the ONE expansion protocol and stained with NHS-ester fluorescein (cyan). Images were acquired with STED microscopy in confocal mode. (d) Shown is a representative image of CD81-positive exosome (green box, left) and CD63-positive exosome (right). $N = 3$ independent experiments.

localization between CD63 and CD81. Specifically, the Pearson's correlation coefficient was as low ast 0.041 ± 0.001 indicating random co-localization and the Manders' overlap coefficients showed similarly low values of 0.054 ± 0.002 for CD81 within CD63 and 0.046 ± 0.003 for CD63 within CD81 (Figure 6b). These data indicated that CD81 and CD63 are localized to distinct exosome subpopulations in murine CTLs.

To further validate this observed heterogeneity and to characterize the two distinct exosome subpopulations, we adapted the 10X expansion protocol of ONE microscopy, typically used for 3D protein structure analysis, for expanding exosomes (Figure 6c) (Shaib et al. 2024). Exosomes pelleted onto gelatin-coated coverslips were fixed and stained with antibodies specific to CD81 and CD63. An acrylamide-based anchor (Acryloyl-X) was applied to attach the lysine residues on the exosome surface to the swellable gel matrix. After hydrolysis through heat treatment, which created breaks in the amino acid chains and thus allowed the isotropic expansion of the sample, they were stained with N-hydroxysuccinimide (NHS) ester fluorescein to label the exposed amino groups generated during homogenization. A 10-fold expansion was achieved through repetitive washing with distilled water. We then imaged the expanded samples for super-resolution radial fluctuations (SRRF) analysis using a four-color STED Quadscan in confocal mode, with 1100 acquired frames (Figure 6d). The ONE platform plugin on ImageJ was used to correct sample drift during acquisition and reconstruct the final image (Shaib et al. 2024).

The expanded exosomes confirmed the previously observed heterogeneity, revealing that CD81 and CD63 mark entirely separate populations of exosomes. Remarkably, we did not observe any exosomes that were double-positive for both CD81 and CD63, reinforcing the finding that these two tetraspanins define distinct

subpopulations. Interestingly, imaging of expanded exosomes revealed a correlation between size and the tetraspanin located to the exosome. CD81 was predominantly associated with smaller exosomes, in the range of 30–80 nm, while CD63 was more commonly found on larger exosomes, ranging from 80–150 nm. This suggests that the size of the exosome may relate to the specific tetraspanins it carries, potentially reflecting distinct origins, functions, or cargo types.

3.7 | CD63 positive Exosome Are Enriched in Apoptotic Proteins

Our results suggest that both subpopulations are distinct in function. To determine their individual protein composition, we did a proteomic analysis of $CD63^+$ and $CD81^+$ exosomes isolated from WT mouse CTLs. As described above, we isolated small EVs from the supernatant of 600–800 × $>10^6$ CTLs via differential ultracentrifugation. They were pelleted at 100,000 × *g*, dissolved in D-PBS and qualitatively purified with mouse anti-CD63 and anti-CD81 conjugated magnetic micro beads and prepared for mass spectrometry analysis (Figure S5a). Isolated EVs were tryptic in gel digested, and analyzed by nano LC TimsTOF analysis. Database search was followed by Quantil-Normalization of the detected protein spectra, where we identified 3627 proteins (Table S4). The number of detected peptides in the $CD63^+$ exosomes were consistently lower compared to $CD81^+$ exosomes. Nevertheless, the quality of the data was proven in a mean intensity box plot, a ridgeline analysis and a mean versus SD analysis (Figure S5b–d). A hierarchical clustering heatmap was generated to visualize the normalized abundance of the expressed proteins across all biological samples (Figure 7a). The comparative analysis identified specific protein signatures associated with each individual group. To assess similarities and differences in the total proteomic dataset of both groups, we performed a principal component analysis (PCA). All biological replicates of isolated groups revealed a clear separation (Figure 7b) reflecting the reproducibility of EV isolation and a robust label-free mass spectrometry analysis. The dendrograms of the correlation heatmap reveal a high degree of similarity within the anti-CD63 and anti-CD81 isolated samples, while concurrently demonstrating a clear distinction between them, thereby confirming the presence of distinct protein profiles (Figure 7c). To ascertain the exosomal origin of the isolated vesicles, we cross-referenced our proteome with the ExoCarta Top 100 proteins (http://exocarta.org/sEV_top100). Of these, 96 were identified in our dataset. Figure 7d displays 19 exosomal proteins, which are enriched in either anti-CD63 (LogFC←1 (CD81/CD63)), or the anti-CD81 isolated samples (LogFC>1 (CD81/CD63) or else in both samples.

We performed a differential expression analysis using a volcano plot (Figure 7e). We found that 297 proteins were significantly enriched in the anti-CD63 isolated samples whereas 309 were enriched in the anti-CD81 samples. For better visualization, we labeled a number of highly enriched proteins, among which we found the CD63 and the CD81 proteins. Intriguingly, we found that the anti-CD63 isolated sample contained a substantial amount of highly enriched proapoptotic proteins. To investigate this in more detail, we generated an apoptosis specific heatmap, and found that while apoptotic markers were found in both samples, they were more abundant in the $CD63^+$ samples (Figure 7f). This finding was also supported by the GO term analysis (Figure S5e–j). The $CD81^+$ group displays many biological processes involved in cell to cell interactions (Figure S5j), especially in the immune-system regulation. In contrast, the $CD63^+$ group display in the molecular functions, a large variety of peptidases and their regulation (Figure S5e) suggesting a role in apoptosis (defense response in biological processes, Figure S5i).

These findings, indicate that exosomes released from CTL might have a function in killing target cells and that $CD63^+$ exosomes might be more effective as those that are $CD81^+$.

3.8 | Munc13-4 KO CTLs Secrete Exosomes With Similar Morphology and Tetraspanin Expression Profile as WT CTLs

To differentiate the putative difference in function of $CD63^+$ and $CD81^+$ exosomes, we decided to use a mouse model, in which exocytosis of lytic granules and MVBs can be separated. As shown exosomes are located in two different organelle types, MVBs containing mainly $CD81^+$ exosomes and MCGs containing mainly $CD63^+$ exosomes (Figure 3). MCGs and an extremely small population of MVBs are secreted in a polarized manner at the IS (Figure 2h, S2). Since Munc13-4 is known to be the priming factor for lytic granules at the IS (Dudenhoffer-Pfeifer et al. 2013; Feldmann et al. 2003), we investigated whether exosome release from MVBs and MCGs is subject to differential regulation by Munc13-4.

We used Munc-13-4 KO mice (*Jinx* mice), which mimic the FHL3 phenotype in humans due to genetic alteration in the *Unc13d* gene, for this investigation. To promote prolonged synapse formation and lytic granule secretion, we incubated day 3 CTLs seeded on anti-CD3ε-coated coverslips in IMDM medium containing 1.49 mM Ca^{2+} for 1 h at 37°C and 5% CO_2. Subsequently we subjected the cells to high-pressure freezing, following freeze substitution with osmium tetroxide contrasting and Epon-embedding. We compared the abundance of SCGs, MCGs, late endosomes (MVBs), and early endosomes (EE) in the area of the formed IS from Munc13-4 KO and WT CTLs (Figure 8a). For this purpose, we determined the organelle density in the one third of the cell that had formed contact with coated glass coverslip. In comparison to WT CTLs, SCGs and MCGs accumulated significantly in this area in Munc13-4 KO CTLs, reflecting the expected secretion defect in these cells (Figure 8b). It was proposed that Munc13-4 might be involved in inter-organelle fusion (Menager et al. 2007). To test this, we compared the organelle diameter of the four organelle types present in the cell sections (Figure 8c) and found no significant differences between WT and Munc13-4 KO CTLs. Additional control EM experiments of both cells groups after short term IS formation within 20 min revealed no differences in organelle density or size (Figure S6a–c).

We postulate that during bead activation for T-cell expansion over 5 days in culture, T-cells form an artificial IS during additional contact with anti-CD3/anti-CD28 coated beads, leading to cytotoxic organelle exocytosis in WT CTLs but not in Munc13-4 KO CTLs. A defect in MCG fusion would reduce the exosome amount in the supernatant. To address this hypothesis,

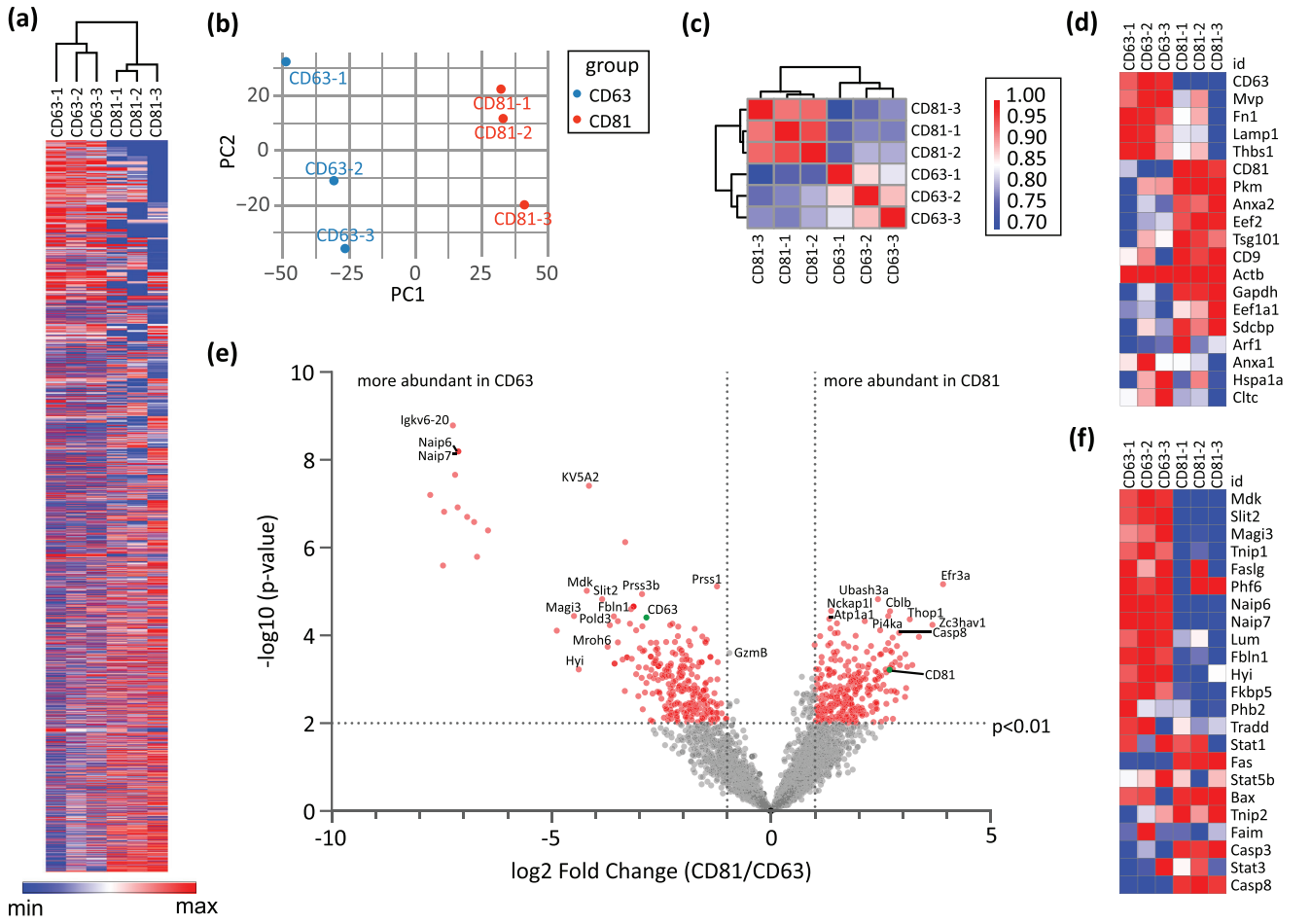

FIGURE 7 | Mass spectrometry analysis of CD63 and CD81 positive exosomes reveal molecular differences. (a) Hierarchical clustering heatmap illustrating all protein abundance values (Log2) of the two groups of 3627 proteins identified after quantile normalization. Dendrogram illustrates the similarity within the biological replicates of each analyzed subtype. Relative color scheme: blue and red for minimum and maximum, respectively. (b) Principal component analysis (PCA). (c) Sample correlation graph shows a similar intra-cluster correlation for CD81 (<0.9) and for CD63 (>0.8). The inter-cluster correlation indicates a clear difference of both groups. (d) Heatmap of specific Top 100 (Exocarta) markers present in the two groups (Log2 of the qn-normalized protein abundance values). Relative color scheme: blue and red for minimum and maximum, respectively. (e) Volcano plot of differentially expressed proteins between both groups. The data is represented as -Log10 (p value) versus Log2 fold change (CD81/CD63) change. Significance is reached by a value of -Log10 (p value) >2 and Log2 fold change (CD81/CD63) >1 or <-1 (Red dots). Green dots display the significant enriched marker proteins CD63 and CD81 for each group. Grey dots show proteins, that are not considered significantly differentially expressed. Proteins in the apoptosis pathway are especially enriched in the CD63$^+$ subgroup (e.g. Naip6, Naip7, Slit2, Magi3, Mroh6 etc.) (f) Heatmap of significantly enriched proteins involved in apoptosis in CD63$^+$ or CD81$^+$ subgroups displayed in the volcano plot shown in (*f*) (red markers). Illustrated are protein abundance values (Log2) with $p < 0.01$ and Log2 fold change (CD81/CD63) >1 or <-1. Relative color scheme: blue and red for minimum and maximum, respectively.

we isolated exosomes from both WT and Munc13-4 KO CTLs using differential sucrose density gradient ultracentrifugation. TEM data demonstrated that both WT and Munc13-4 KO CTLs secrete exosomes, indicating that exosome release can occur independently of Munc13-4 (Figure 8d). The analysis of exosome diameter revealed no significant differences between the two groups, with an average diameter of 76.59 ± 1.92 nm for WT-derived exosomes and 75.89 ± 2.44 nm for Munc13-4 KO-derived exosomes (Figure 8e), suggesting that Munc13-4 does not influence the maturation of exosomes in murine CTLs. However, the exosome yield from Munc13-4 KO CTLs was reduced by 18.13% compared to WT starting with a comparable number of CTLs in culture (Figure 8f). We then examined whether Munc13-4 KO induced a specific reduction in one of the exosome subpopulations by staining the exosomes isolated from WT and KO CTL cell culture supernatants with anti-CD63 and anti-CD81 antibodies (Figure 8g). Object based colocalisation analysis performed after segmentation with Cellpose 2.0 (Pachitariu and Stringer 2022) revealed a significant reduction by about 13% in the CD63$^+$ exosomes subpopulation and a corresponding increase in the CD81$^+$ exosomes subpopulation in Munc13-4 KO compared to WT CTL derived exosomes (Figure 8h). To further investigate whether the secretion of MCGs is Munc13-4-dependent, we conducted TIRF microscopy acquisition on Munc13-4 KO CTLs overexpressing CD63-pHuji and CD81-SEP. The experiments were performed under the same conditions as described above, but with an imaging time elongated to 30 min. No fusion events were observed during the time of acquisition, confirming that MCG secretion is Munc13-4 dependent (Figure S7a). Since MVB secretion was rarely observed at the IS (Figure 2h), we suggest that MVB secretion might occur independently of Munc13-4, in an unpolarized manner outside the IS. This is supported by the

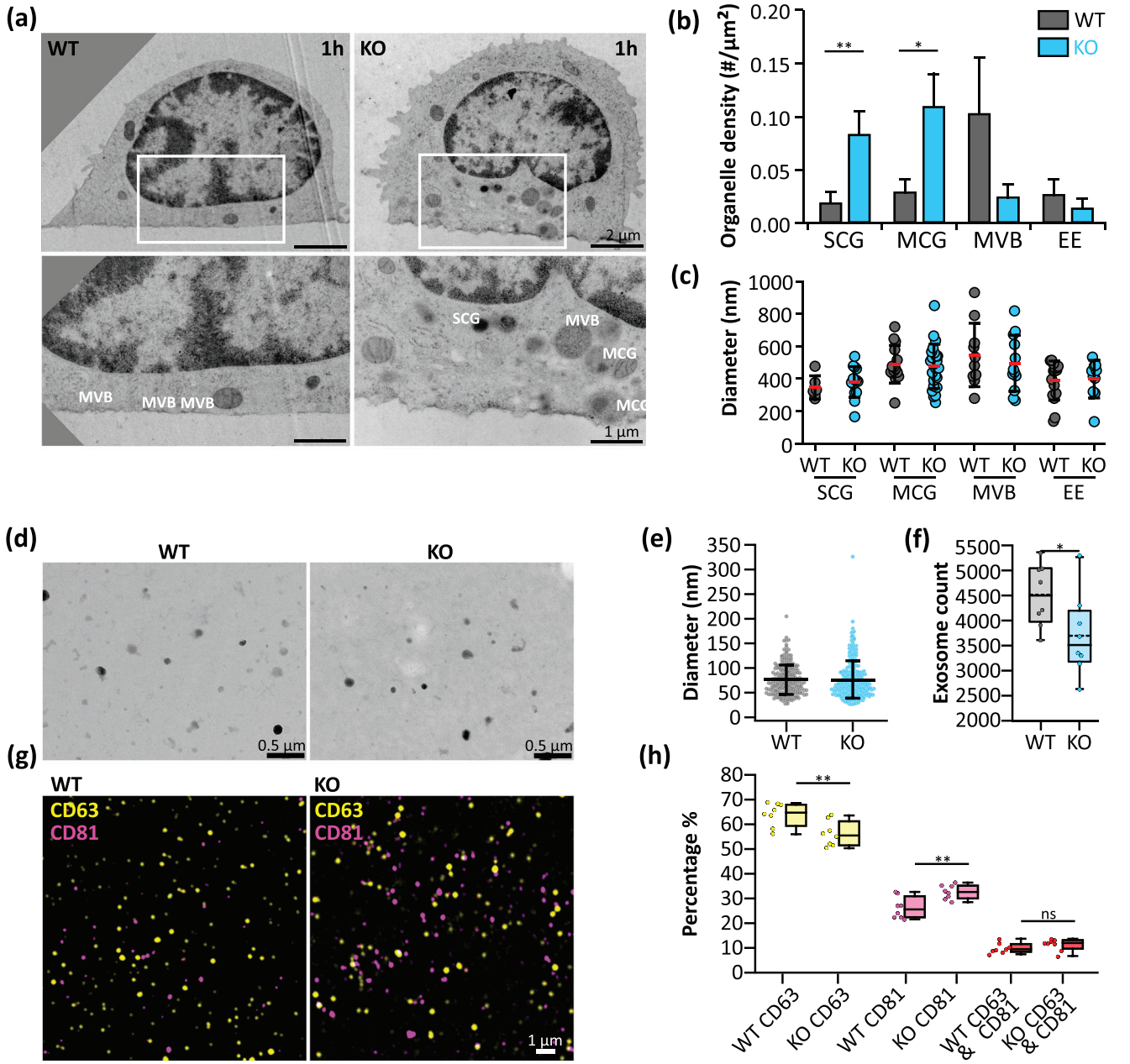

FIGURE 8 | Comparison of Munc13-4 and WT CTLs, organelles and exosomes. (a) Representative electron micrographs of WT (left) and Munc13-4 KO CTL (right). To form a prolonged immunological synapse (IS) cells were incubated for 1 h on anti-CD3ε coated sapphire disc before high-pressure freezing and resin embedding. Upper row shows overview images of cells with marked regions (white rectangle) magnified in the images shown in the lower row. MVB, multivesicular body; SCG, single core granule; MCG, multi core granule. (b) Organelle density of cytotoxic organelles (SCG and MCG) and late and early endosomes (MVB and EE, respectively) in WT and Munc13-4 KO CTLs as shown in (*a*) (upper row). Density was calculated in the third of the cell area, forming a contact with the coated sapphire disc, recognizable by the straight edge of the cell. $N_{mice} = 2$, WT $n_{cells} = 18$, Munc13-4 KO $n_{cells} = 18$. Mann–Whitney *U* test was used to compare values. Data given as mean ± SEM, $^{**}p = 0.009$, $^{*}p = 0.021$. (c) Diameter of cytotoxic organelles (SCG and MCG) and late and early endosomes (MVB and EE) present in the cells as shown in (*a*). $N_{mice} = 2$, WT $n_{cells} = 18$, Munc13-4 KO $n_{cells} = 18$. Data are given as mean (red line) and STD (black error bars). (d) Representative electron micrographs of exosomes isolated from WT CTLs (left) or Munc13-4 KO CTLs (right). $N = 3$ (e) Scatter dot plot analysis of the exosome diameter as shown in (*d*) isolated from WT or Munc13-4 KO CTLs. (f) Box plot showing the number of exosomes isolated from WT or Munc13-4 KO CTLs' supernatant. Value corresponds to the number of exosomes per fields of view each sized 75.56 × 75.40 µm. (g) Representative structured illumination microscopy (SIM) images of exosomes isolated from WT (left) or Munc13-4 KO CTLs (right), centrifuged on gelatin-coated coverslips, fixed, and stained with anti-CD63 (yellow) and anti-CD81 (magenta) antibodies. Shown are the images of the merged channels. (h) Object-based co-localization analysis of CD63 alone (yellow), CD81 alone (magenta), and the co-localization of CD63 and CD81 (red) displayed as a scatter dot plot with the values superimposed with a box plot comprising the median (line). $N_{gradients} = 3$, from three independent experiments. Data represented as mean ± SEM, and data significance was analyzed by the student's *t*-test, $^{*}p < 0.05$, $^{**}p < 0.01$, ns: not significant.

fact that Munc13-4 KO CTLs are surrounded by exosomes after 30 min incubation on anti-CD3ε coated coverslips (Figure S7b,c)

Our results indicate that exosomes secreted at the IS are enriched in CD63 and that they are derived from MCGs, which are secreted in a Munc13-4-dependent manner. In contrast, $CD81^+$ exosomes appear to be enriched in MVBs and are secreted in a Munc13-4-independent manner, likely outside the IS.

3.9 | Polarised exosomes, released in a Munc13-4-dependent manner, support the killing of target cells via the caspase 3 pathway

The biological effects of T cell-derived exosomes on tumor cell lines are still not well understood. We investigated the physiological effect of exosomes derived from WT CTLs on P815 cells and compared it with the effect of exosomes released from Munc13-4 KO cells. The aim was to distinguish the role of exosomes secreted by MVBs from that of MCGs, as they are not released by Munc13-4 KO CTLs. Flow cytometric analysis of cell viability, activation state, and subtype distribution showed no significant differences between the cells with these two different genetic backgrounds (Figure S3). Freshly isolated (less than 24 h storage at 4°C no freezing) exosomes from both WT and Munc13-4 KO CTL supernatants were incubated with P815 tumor cells for 12 and 24 h. After incubation, P815 cells were analyzed using flow cytometry to assess caspase 3 activation and propidium iodide (PI) staining, typical markers of early apoptosis and cell membrane integrity, respectively (Figure 9a). Caspase 3 activation is considered as a key end-point of the apoptosis process activating the final stage of programmed cell death (Bedoui et al. 2020). After 12 h of incubation, we observed a notable difference in apoptotic activity between exosomes derived from WT and Munc13-4 KO CTLs. Caspase 3 activation was observed in 33.06 ± 1.27% of P815 cells treated with WT exosomes, which was significantly higher compared to the 15.53 ± 0.49% observed in cells treated with Munc13-4 KO exosomes (Figure 9b). This suggests that exosomes released from WT CTLs are more potent in inducing apoptosis in P815 tumor cells than those from Munc13-4 KO CTLs, lacking MCG-derived exosomes. The percentage of cells double-positive for both PI and cleaved caspase 3, indicating cells in the later stages of apoptosis, was identical for both groups, with 6.5 ± 1.2% for WT and 6.5 ± 0.1% for KO (Figure 9b). After 24 h of incubation, the effects of the isolated exosomes on P815 cells became more pronounced as the number of cells showing caspase 3 activation nearly doubled to 57.0 ± 3.4% in the WT group, while those double positive for cleaved caspase 3 and PI increased to 9.2 ± 1.4%. However, the difference between WT and Munc13-4 KO exosomes remained remarkably consistent. In fact, the percentage of cleaved caspase 3-positive P815 tumor cells treated with WT exosomes was still twice as high as those treated with Munc13-4 KO exosomes, and the percentage of cleaved caspase 3 and PI double-positive P815 cells was identical in both groups (Figure 9c). These results indicate that MCG-derived exosomes, enriched with CD63, show a strong cytotoxic effect on target cells, highlighting functional differences between exosomes from different organelles within CTLs. Furthermore, the significant increase in caspase 3-positive cells from 12 to 24 h in both WT and KO conditions suggests a progressive accumulation of apoptotic signals over time, emphasizing the sustained and enhanced cytotoxic potential of exosomes over extended periods.

4 | Discussion

Murine and human T-cells contain different types of organelles bearing ILVs, the well-known MVBs as the origin of exosomes and MCGs, a newly characterized cytotoxic organelle containing SMAPs and other small ILVs (Balint et al. 2020; Cassioli et al. 2025; Chang et al. 2022). In this study we have established and utilized a variety of techniques, including a newly developed bead-activated effector primary T-cell expansion culture of WT and Munc13-4 KO mice to ensure sufficient quantities of exosomes for acute analysis, adapted sucrose density ultracentrifugation to isolate distinct exosome and organelle fractions, direct immunostaining of isolated organelles and exosomes using coverslip centrifugation, apoptosis assay using flow cytometry and high-resolution SI-, TIRF-, electron and 10x expansion (ONE) microscopy. With these techniques we analyzed the heterogeneity of primary mouse T-cell derived exosomes in MVBs and MCGs, starting from their localization in these organelles, via their release especially at the IS, the exosome morphology and their protein composition up to their physiological effect on cancer cells.

Exosomes are per definition originating from MVBs. While this definition applies to most cell types, the situation is somewhat more complex in CTLs where a new type of lytic granules, the MCGs, have been described (Chang et al. 2022). MCGs were defined as SMAP-containing organelles and we showed with the present work that they also contain ILVs (Figure 1). Due to their mixed content (Gzm, perforin and ILVs) one could envision the MCG as a biogenesis intermediate between MVB and the classical lytic granule, namely the SCG. However, mass spectrometry data indicated that MCGs might stem from a different origin as the SCGs (Chang et al. 2022). In fact, protein composition from SCGs indicated a lysosomal origin while that of MCGs pointed toward an endosomal origin. Therefore, the MCGs are closer to MVBs than to SCGs (Arya et al. 2024; Cassioli and Baldari 2022). This hypothesis is supported by the fact that SCGs harbor mainly CD63 on their membrane while a large majority of MCG and MVBs membrane contain mainly CD81 (Figure 4). The question that arises is whether MCGs and MVBs are the same organelles. Lettau and Janssen (2021) proposed that exosomes are released from dense and light MVBs, which in analogy to our results would correspond to our MCGs and MVBs, respectively. Several lines of evidence argue against this hypothesis: (1) MCGs contain Gzm, perforin, TSP-1 and 4 assembled in SMAPs (Balint et al. 2020; Cassioli et al. 2025; Chang et al. 2022). None of these proteins are found in MVBs; (2) Their fusion occurs at different sites. MCGs are exclusively exocytosed at the IS in a stimulation dependent manner (Figure S2, (Chang et al. 2022)). In contrast, the MVBs likely fuse elsewhere on the plasma membrane as less than 4% of the $CD63^+$ or $CD81^+$ fusion events at the IS stemmed from MVBs (Figure 2); (3) MVBs and MCGs fusion mechanism is different. Gzm and perforin release is completely obliterated in Munc13-4 KO human and mouse CTL (Figure S7, Dudenhoffer-Pfeifer et al. 2013; Feldmann et al. 2003). Thus, MCG fusion releasing Gzm and perforin is entirely Munc13-4 dependent. In contrast unpolarized exosome release still occur normally in Munc13-4 KO cells (Figure 8), indicating that MVB fusion is Munc13-4

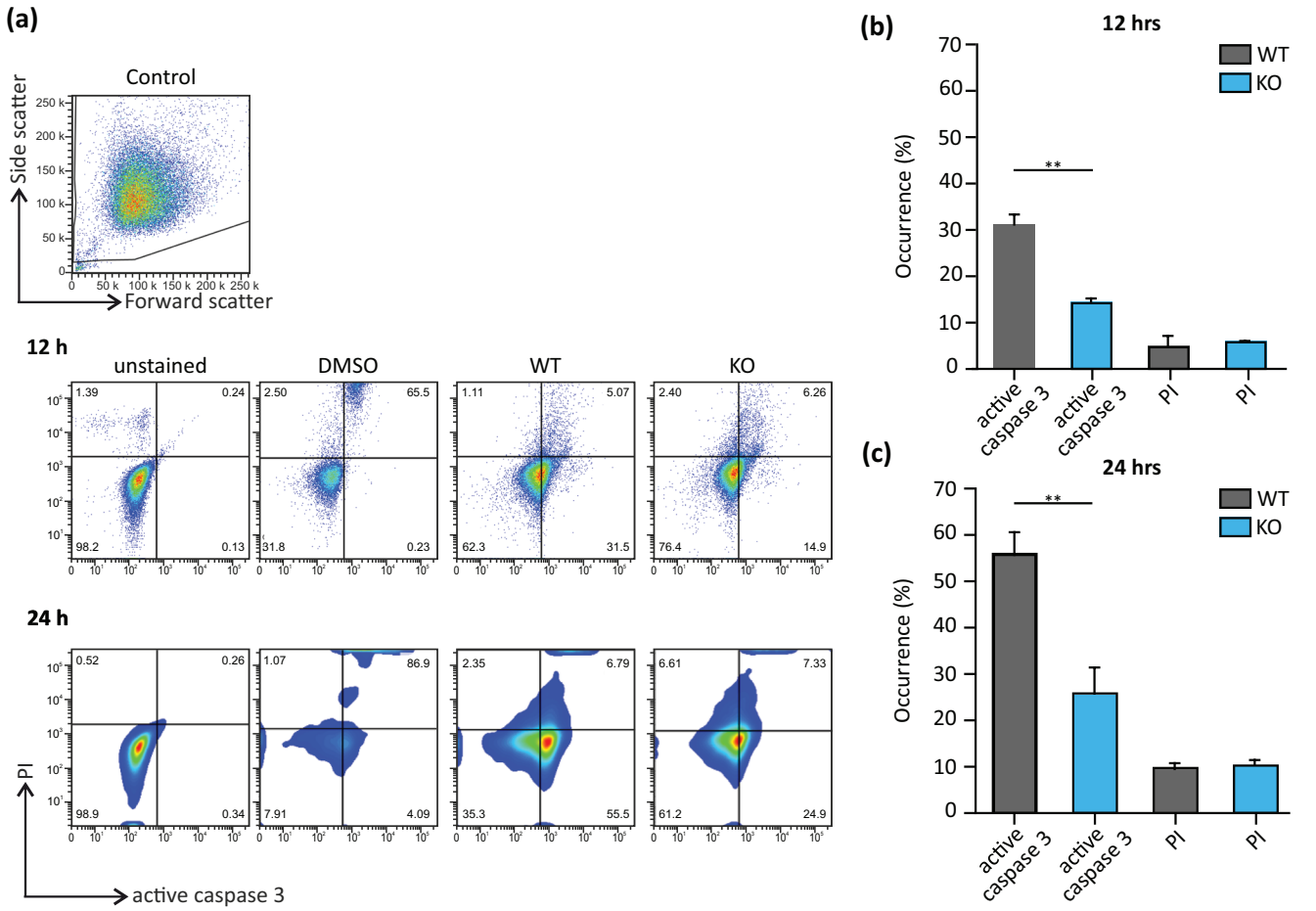

FIGURE 9 | Cytotoxicity and molecular mechanisms involved in killing of P815 tumor cell lines by CTL-derived exosomes. Cytotoxic assay on P815 target cells incubated with 10 μg/mL WT or Munc13-4 KO-derived exosomes. (a) Representative flow cytometry analysis of the cytotoxic activity of CTL-derived exosomes. Cells were gated based on the forward and side scatter. DMSO was used as a positive control. The percentage of active caspase 3 and PI/caspase 3 double positive cells was evaluated after 12 (b) and 24 h (c) of incubation with CTL-derived exosomes. $N = 3$, from three independent experiments. Data represented as mean ± SEM, $^{**}p < 0.01$.

independent; (4) The stimulus for MCG and MVB fusion is likely different. Lytic granule (i.e. also MCG) fusion with the plasma membrane is specifically triggered by the IS formation and the ensuing intracellular Ca^{2+} increase (Martina et al. 2011; Stinchcombe et al. 2006). The situation is not as clear for MVB fusion. While Lettau et al. showed that the dense MVB were released upon co-increase of intracellular Ca^{2+} concentration and PKC activation, light MVB were released upon weaker stimulus such as PKC activation alone (Lettau et al. 2019; Lettau and Janssen 2021). As strong increase of Ca^{2+} concentration is confined to the IS (Quintana et al. 2011), PKC activation is a better candidate to trigger the fusion of MVBs releasing non-polarized exosomes away from the IS. In conclusion, MVBs and MCGs are two different types of organelles, whereby the MCGs are a hybrid organelle between SCGs and MVBs.

Recent studies have shown that EVs from different cell types have different combinations and amounts of CD63 and CD81 on their surface (Andreu and Yanez-Mo 2014; Kowal et al. 2016; Rydland et al. 2023). We expected that these tetraspanins co-localize within exosome-bearing organelles, MCGs and MVBs, in murine CTLs. CLEM analysis revealed that both MVBs and MCGs contain CD63 and CD81, with CD81 serving as a more specific marker for these organelles in comparison to CD63 (Figure 1). In addition, GzmB is restricted to the electron-dense regions of MCGs, indicating its preferential association with SMAPs rather than with ILVs (Balint et al. 2020). These findings suggest MCGs as additional organelles containing ILVs that are distinct from those contained in the classical MVBs. This implies heterogeneous release mechanisms and functional differentiation in immune modulation of the MCG and MVB-derived exosomes. Given their specific release at the IS, it is plausible that exosomes derived from MCGs in $CD8^+$ T-cells may contribute to or represent a form of trans synaptic EVs, akin to those recently described for $CD4^+$ T-cells by Cespedes et al. (2022).

Since most, if not all, cell types release exosomes with important functional impacts, understanding the mechanism of exosome biogenesis and release kinetics is essential for elucidating their physiological roles in vivo. The tetraspanin CD63 has been widely used for real-time visualization of exosome release from parental cells (Verweij et al. 2018). Consistent with previous reports identifying CD63 as a general marker for secretory lysosomes in CTLs (Metzelaar et al. 1991; Peters et al. 1991) we revealed a high co-localization of CD63 with GzmB (Figure 1b), with CLEM analysis and immunocytochemistry of isolated organelles

(Figure 4), suggesting an association of CD63 with SCG membrane. We took advantage of the fact that CD63 is a pan marker in CTLs to simultaneously visualize $CD63^+$ fusion events of MVBs, MCGs, and SCGs at the IS in real-time using TIRF microscopy and to quantify their respective release abundance based on their kinetic properties. SCGs, containing soluble cargo such as GzmB and perforin, displayed fast fusion dynamics with fusion events lasting less than 2 s, marked by fast fluorescence spike and decay (Figure 2a,b). These dynamics align with previous reports of plasma membrane deposition of VAMP2 from SCGs (Estl et al. 2020; Verweij et al. 2018). In contrast, MCG and MVB fusion events exhibited longer CD63 signal durations of more than 2 s (Figure 2c,d), in agreement with previously reported longer MVB fusion dynamics observed in Hela cells and A549 cells (Mahmood et al. 2023; Verweij et al. 2018). These observations confirm the identity of these organelles as MVBs/MCGs. The extended signal duration may be attributed to exosome entrapment between the cells and the glass coverslip or their immobilization by adhering to the plasma membrane (PM) after fusion. This hypothesis is reinforced by the fact that the decay time of CD63 on supported lipid bilayer (SLB) was in general faster than its decay time on glass coverslips (Figure S1e). Our TIRF microscopy data revealed that, out of the long fusion events, the main fraction detected at the IS corresponded to MCGs, whereas only a minor fraction represented MVBs, identified by their absence of GzmB (Figure 2h).

A more detailed characterization of MCGs after overexpression of CD81-SEP and CD63-pHuji in WT CTLs revealed a heterogeneous fusion profile in TIRF microscopy (Figure 3). During MCG fusion events at the IS, the decay time of CD81 was consistently faster than that of CD63 (Figure 3g). We explained this by a higher association of CD81 to the MCG organelle membranes than on ILVs and we confirmed this hypothesis, by specific membrane staining of isolated organelles (Figure 4e). However, CD63 with longer decay times is then predominantly present on ILVs in MCGs (Figure 3f).

We further elucidated the regulatory mechanisms governing exosome secretion by investigating Munc13-4, a critical protein involved in granule fusion at the IS (Dudenhöffer-Pfeifer et al. 2013). Specifically, we were interested whether this priming factor equally promotes the fusion of both ILV-containing organelles, MVBs and MCGs. Electron microscopy confirmed normal morphology and biogenesis of cytotoxic granules, early and late endosomes and IS formation in the *Jinx* mouse (Crozat et al. 2007). Now we showed that the MVB, MCGs and exosomes derived from KO-CTL cultures have comparable size to those of WT suggesting a Mun13-4 independent biogenesis through endosomal sorting complexes required for transport (ESCRT) dependent mechanisms in mouse cells (Figures 8a,b, S6). This finding contrasts with a previous study in which Munc13-4 KO MDA-MB-231 cancer cells showed increased MVB size (Messenger et al. 2018) and an effect on cytotoxic granule maturation in human CTLs (Menager et al. 2007). The accumulation of both MCG and SCG at the IS after prolonged synapse formation suggests that MCG fusion, as well as SCG, is Munc13-4 dependent. TIRF analysis of Munc13-4 KO CTLs co-expressing CD81-SEP and CD63-pHuji showed no secretion at the IS, confirming MCG fusion dependence on Munc13-4 (Figure S7a). The exosome yield from Munc13-4 KO CTL supernatant was decreased by about 18% in comparison to WT. Our culture condition includes continuous stimulation of the CTL with anti-CD3/anti-CD28 coated beads that induce SCG and MCG exocytosis, which should not occur in Munc13-4 KO CTLs. This suggests that there is a Munc13-4 independent release of a specific subpopulation of exosomes from MVBs (Figure 8f) secreted in a non-polarized fashion. Interestingly, $CD81^+$ and $CD63^+$ exosomes accumulated on the coverslip near transfected cells, indicating non-polarized exosome release from MVBs (Figure S7b,c). These results indicate that MCGs appear to preferentially release their ILVs directly at the IS possibly as trans synaptic EVs, enabling a focused interaction with target cells. In contrast, non-polarized MVBs likely enable broader, less targeted release of exosomes, allowing $CD8^+$ CTLs to communicate systemically. The balancing of local and systemic immune responses highlights the specialized intracellular organization and the highly coordinated role of exosomes in immune regulation in CTLs.

Most of previous studies have focused mainly on comparative analysis of classic EV subtypes including a mixture of apoptotic bodies, microvesicles, and exosomes released by different cell types (Breitwieser et al. 2022; Kowal et al. 2016; Lunavat et al. 2015; Xu et al. 2015) and of EVs being released from the apical and basolateral surfaces of organoids (Tauro et al. 2013), rather than on the exosomes themselves. To address the difference in tetraspanin localization we used freshly isolated exosomes from the supernatant of primary murine CTLs. Isolating exosomes from these cell cultures is significantly more challenging than using immortalized cell lines due to the requirement for sustained, high-quality cell cultures with minimal cell death over several days. To ensure purity, we used a combination of differential ultracentrifugation and an adapted sucrose density gradient ultracentrifugation method (Figure 5a), isolating exosomes based on their size and density (Bobrie et al. 2012; Thery et al. 2006). We validated the identity and the size of isolated exosomes with Western blotting for exosome markers ALIX and TSG101 (Figure 5c) and by electron microscopy. Proteome profiling confirmed exosome purity, with 79 detected proteins included in the Exocarta top 100 list. Low abundance of Golgi, mitochondrial, and nuclear proteins further supports this purity (Figure 5e,f). With these purified exosomes we investigated whether CD81 and CD63 co-localize on the same exosome or mark distinct subpopulations. The conventional assumption is that EVs are homogenously containing several tetraspanins together (Kim et al. 2022; Welsh et al. 2024). In contrast, we found that in CTLs, CD63 and CD81 rarely co-localize on individual exosomes, revealing at least two distinct exosome subpopulations in mouse CTLs (Figure 6a,b). An interesting observation from the TEM analysis of isolated exosomes was the existence of two different size populations (Figure 5b). Using the ONE microscopy technique, we found that there is a relationship between exosome size and surface markers, since CD63-positive exosomes tended to be larger than CD81-positive ones (Figure 6c,d). Our detailed differential proteomic study of immune-isolated $CD63^+$ and $CD81^+$ exosome from WT CTLs confirmed that there is a clear difference in cargo in the two subtypes. While $CD63^+$ exosomes are enriched in typical regulatory and pro-apoptotic proteins, $CD81^+$ exosomes contain more proteins involved in immune regulation (Figures 7 and S5). Since tetraspanins are involved in the process of sorting cargo such as proteins and miRNAs (Andreu and Yanez-Mo 2014; Perez-Hernandez et al. 2013; Rana et al. 2012; van Niel et al. 2011), our

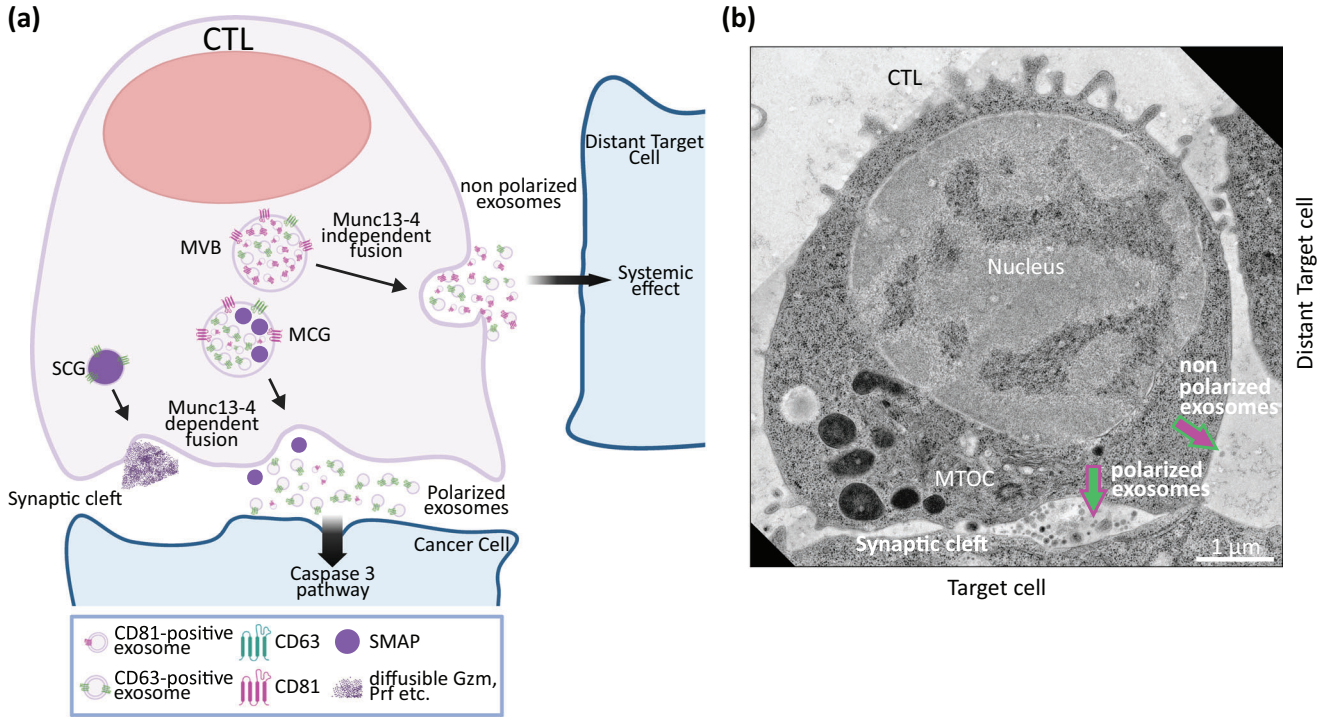

FIGURE 10 | Model showing the differential killing by polarized and non-polarized exosomes. (a) Suggested model summarizing our findings. In murine CTLs, exosomes are contained in two distinct organelles, multivesicular bodies (MVBs) and multi core granules (MCGs). Exosomes contained in MCGs are polarized to the immune synapse and are released in a Munc13-4 dependent manner. Non-polarized exosomes are contained in MVBs and are secreted elsewhere throughout the cells in a Munc13-4 independent manner. Exosome killing efficiency is shown as thickness of the black arrows delineating that polarized exosomes show superior killing to their non-polarized counterparts. As depicted CD81 is a more specific marker to exosome containing organelles, due to its abundance on the membrane of MCGs and MVBs and its absence from the membrane of SCGs. Finally, exosomes could be further divided based on their tetraspanin surface expression into CD81-positive exosomes, and CD63-positive exosomes. Where CD63 seems to be abundant on the polarized exosomes and CD81 on the non-polarized ones. Generated by Biorender (https://app.biorender.com/illustrations/670d42a698329c882bc8c70c). (b) Exemplary electron micrograph of a CTL forming an immunological synapse (IS) with a P815 target cell. A second target cell is more distant from the CTL. Exosomes are found abundantly in the synaptic cleft at the IS as indicated by the green filled and magenta outlined arrow. Non-polarized exosomes can be found in the surrounding of the CTL as indicated by the magenta filled and green outlined arrow. The color code of the arrow corresponds to the tetraspanins shown in (*a*). MTOC, microtubule organizing center.

results indicate that exosomes secreted from MCGs and MVBs may differ in size, function, and cargo types.

Differential mass spectrometry analysis of anti-CD63- and anti-CD81-isolated exosomes revealed clear differences between the two types, thereby adding considerable information to our study. We also observed that the exosomes obtained through anti-CD63- and anti-CD81-based enrichment contained more proteins than the highly pure exosomes, which we isolated using sucrose density gradient ultracentrifugation. Notably, we detected a significant quantity of immunoglobulins, potentially originating from the beads employed for isolation. Furthermore, we detected GzmB, TSP1 and TSP4, which are typical SMAP markers, in both the $CD63^+$ and $CD81^+$ groups. SMAPs may bind to exosomes via their surface integrins and be pulled down by antibodies coupled to the beads. This unspecific binding is prevented during sucrose density gradient ultracentrifugation where SMAP markers were not significantly detected (Figures 5 and S4). Therefore, we used these highly pure exosomes in all functional assays.

CTLs may coordinate EV and exosome-mediated signaling for both local and systemic immune response via MCGs and MVBs, respectively. It has been shown that T-cell-derived EVs play a role in immunomodulation, particularly by mediating information exchange between immune cells and tumor cells. For example, the bystander T-cell activity can be downregulated through exosome-mediated signaling (Li et al. 2017). Our data showed that $CD81^+$ exosomes contain large amounts of proteins involved in lymphocyte activation and the regulation of immune processes, as well as cell activation more generally. Therefore, we suggest that these exosomes are used primarily by CTLs for communication. A direct effect of CTL-derived EVs on killing cancer cells has not yet been clearly demonstrated, although initial studies provide an indication (Lu et al. 2022; Zhang et al. 2024). Many studies have focused on a mixture of sEVs, without isolating exosomes for more specific analyses. To address this gap and to investigate the specific effect of MCG-derived exosomes, we studied the physiological effect of freshly isolated exosomes from supernatants of bead-activated effector WT and Munc13-4 KO CTLs on P815 mastocytoma cell line as a tumor model. WT and Munc13-4 KO CTL-derived exosomes induced substantial cytotoxic activity in target cells within 12 h of incubation, with an enhanced effect observed after 24 h (Figure 9a–c). While the impact on late apoptosis or necrosis was comparable between the two groups, exosomes released from WT CTLs displayed significantly higher

effect on early apoptosis than those isolated from Munc13-4 KO CTL. Considering the reduction by 18% of exosome yield in Munc13-4 KO CTLs culture, we can assume that about 20% of the exosomes originates from MCGs while about 80% originates from MVBs in WT culture. The activation of caspase 3 was more than twice as high in WT than in Munc13-4 KO exosomes. Together this indicates that MCG-derived exosomes induce apoptosis about 5-fold higher than MVB-derived exosomes. The effect of these exosomes peaked early on since the difference between Munc13-4 and WT exosomes was similar between 12 and 24 h. We therefore hypothesize that exosome sorting and function are highly specialized in CTLs. Prf1 and GzmB are principal cytotoxic components of SMAPs, the killing entity localized within MCGs (Balint et al. 2020; Chang et al. 2022). The absence of typical SMAP markers from the sucrose density gradient isolated exosomes confirmed that the observed cytotoxic effect of the exosomes is independent of SMAPs. It has been shown that FasL, a transmembrane protein present on EV surfaces, is essential for inducing target cell apoptosis by binding to Fas receptors and triggering caspase-mediated signaling (Alonso et al. 2011; Lu et al. 2022; Monleon et al. 2001; Zuccato et al. 2007). FasL was detected in both purified subtypes of exosomes (Figure 7f). We propose that the remaining activation of caspase 3 by Munc13-4 KO derived exosomes is primarily due to FasL. Exosomes contain a variety of molecules, including proteins, lipids, and nucleic acids such as DNA, RNA, and non-coding RNAs, including microRNAs (miRNAs). miRNAs are key post-transcriptional modulators of gene expression and can be transferred via exosomes to acceptor cells and evoke apoptosis (Guay et al. 2019; Valadi et al. 2007). MCG-derived exosomes are predominantly $CD63^{+}$. Our mass spectrometry analysis (Figure 7f) revealed that they contain a high level of pro-apoptotic proteins such as Bax, FKBP5, Frmd5, and Lum (Nagata and Tanaka 2017; Vij et al. 2005; Yin et al. 2024), as well as apoptosis regulator proteins such as Slit2, Magi3, and Naip6 and 7 (Kaur et al. 2019; Kotelevets and Chastre 2021; Maier et al. 2002). Furthermore, they contained RNA binding proteins (e.g. Mvp, Hnrnpa2b1, Hnrnpm, Hsp90ab1 (see Table S4)). Consistent with our data, Cespedes et al. (2022) showed that trans-synaptic EVs, contain a higher miRNA content than unpolarized EVs. Finally, we also identified IFNγ and chemokine receptors on these exosomes (Table S4). Further investigation is required to understand the impact of the specific proteins, additional cytokines and receptors, as well as miRNA involved in triggering apoptosis in the target cells on the cytotoxic efficiency of T-cell-derived exosomes.

5 | Conclusion

CTLs employ serial killing and additive cytotoxicity through multiple sublethal hits on target cells (Chang et al. 2016; Prager et al. 2019; Weigelin et al. 2021). Based on our new findings, they may utilize both ILVs and SMAPs within MCGs to enhance their cytotoxic arsenal against tumor cells. This study highlights the functional differentiation between polarized and non-polarized exosome populations, demonstrating distinct levels of cytotoxicity (Figure 10). Future research is needed to examine the biogenesis and additional components of polarized MCG-derived exosomes, to unravel their potential function in supporting target cell killing and cancer therapy. We postulate that the additional presence of "cytotoxic" exosomes in MCGs present in human CTLs and NK cells offers a tremendous potential for immunotherapeutic strategies: The next generation of human CAR-T-cells, loaded with therapeutic molecules such as microRNAs in MCG-derived exosomes could exert additional direct cytotoxic effects on cancer cells. Simultaneously, MVB-derived exosomes within these modified CAR-T-cell could modulate the tumor environment, offering a dual approach to tumor targeting and treatment.

Author Contributions

Nadia Alawar: methodology, data curation, writing – original draft, writing – review and editing, formal analysis, visualization, investigation, conceptualization. Claudia Schirra: conceptualization, investigation, methodology, data curation, supervision, writing – original draft, writing – review and editing, visualization, formal analysis. Ruth Rasuli: data curation, investigation, formal analysis. Claudia Fecher-Trost: investigation, data curation, formal analysis, funding acquisition, writing – review and editing. Lisa Weins: investigation, formal analysis. Markus R. Meyer: funding acquisition, resources. Veit Flockerzi: supervision, funding acquisition, writing – review and editing, resources. Andreas Keller: data curation, formal analysis. Michael L. Dustin: writing – review and editing, writing – original draft, funding acquisition, supervision. Jens Rettig: funding acquisition, supervision, conceptualization. Ute Becherer: data curation, formal analysis, visualization, supervision, project administration, writing – original draft, writing – review and editing, conceptualization, funding acquisition.

Acknowledgements

This work was supported by grants from the Deutsche Forschungsgemeinschaft, collaborative research center (SFB 894 (ID number 157660137), subproject A9 (to U.B.), A10 (to J.R.), and A14 (to V.F.)), ID number 203827099 (to V.F.), ID number 469256325 (to M.R.M., Homburg) and ID number 445684568 (to C.F.-T.). European Commission (ERC-2021-SyG_951329 to the Department of Cellular Neurophysiology, Saarland University and M.L.D.). We thank Abed A. Chouaib for providing software tools for imaging analysis, Elmar Krause for support in imaging techniques (SFB894 (P1)). We thank Margarete Klose, Anja Bergsträßer, Nicole Rothgerber, and Katrin Sandmeier for excellent technical assistance. We thank Prof. Frederik J. Verweij for kindly gifting the CD63 and C81 constructs.

Open access funding enabled and organized by Projekt DEAL.

Ethics Statement

All experimental procedures were approved and performed in accordance with the regulations of the state of Saarland (Landesamt für Verbraucherschutz, AZ: 2.4.1.1).

Conflicts of Interest

The authors declare no competing interests.

Data Availability Statement

Mass spectrometry data are available in Tables S2–S4. The mass spectrometry proteomics data have been deposited to the ProteomeXchange Consortium via the PRIDE (Deutsch et al. 2023; Perez-Riverol et al. 2025, 2016) partner repository with the dataset identifier PXD070419 and PXD064012 and via https://doi.org/10.6019/PXD070419, https://doi.org/10.6019/PXD064012. Additional data and information that support the findings of this study is available on Zenodo with restricted access (https://doi.org/10.5281/zenodo.18024516). The data will be made available by the corresponding author upon reasonable request.

References

Alawar, N., C. Schirra, M. Hohmann, and U. Becherer. 2024. "A Solution for Highly Efficient Electroporation of Primary Cytotoxic T Lymphocytes." *BMC Biotechnology [Electronic Resource]* 24: 16. https://doi.org/10.1186/s12896-024-00839-4.

Alonso, R., C. Mazzeo, M. C. Rodriguez, et al. 2011. "Diacylglycerol Kinase Alpha Regulates the Formation and Polarisation of Mature Multivesicular Bodies Involved in the Secretion of Fas Ligand-containing Exosomes in T Lymphocytes." *Cell Death and Differentiation* 18: 1161–1173. https://doi.org/10.1038/cdd.2010.184.

Alspach, E., D. M. Lussier, and R. D. Schreiber. 2019. "Interferon Gamma and Its Important Roles in Promoting and Inhibiting Spontaneous and Therapeutic Cancer Immunity." *Cold Spring Harbor Perspectives in Biology* 11: a028480. https://doi.org/10.1101/cshperspect.a028480.

Andreu, Z., and M. Yanez-Mo. 2014. "Tetraspanins in Extracellular Vesicle Formation and Function." *Frontiers in Immunology* 5: 442. https://doi.org/10.3389/fimmu.2014.00442.

Arya, S. B., S. P. Collie, and C. A. Parent. 2024. "The Ins-and-Outs of Exosome Biogenesis, Secretion, and Internalization." *Trends in Cell Biology* 34: 90–108. https://doi.org/10.1016/j.tcb.2023.06.006.

Balint, S., S. Muller, R. Fischer, et al. 2020. "Supramolecular Attack Particles Are Autonomous Killing Entities Released From Cytotoxic T Cells." *Science* 368: 897–901. https://doi.org/10.1126/science.aay9207.

Bedoui, S., M. J. Herold, and A. Strasser. 2020. "Emerging Connectivity of Programmed Cell Death Pathways and Its Physiological Implications." *Nature Reviews Molecular Cell Biology* 21: 678–695. https://doi.org/10.1038/s41580-020-0270-8.

Bobrie, A., M. Colombo, S. Krumeich, G. Raposo, and C. Thery. 2012. "Diverse Subpopulations of Vesicles Secreted by Different Intracellular Mechanisms Are Present in Exosome Preparations Obtained by Differential Ultracentrifugation." *Journal of Extracellular Vesicles* 1: 18397. https://doi.org/10.3402/jev.v1i0.18397.

Bolte, S., and F. P. Cordelieres. 2006. "A Guided Tour Into Subcellular Colocalization Analysis in Light Microscopy." *Journal of Microscopy* 224: 213–232. https://doi.org/10.1111/j.1365-2818.2006.01706.x.

Bossi, G., and G. M. Griffiths. 1999. "Degranulation Plays an Essential Part in Regulating Cell Surface Expression of Fas Ligand in T Cells and Natural Killer Cells." *Nature Medicine* 5: 90–96. https://doi.org/10.1038/4779.

Breitwieser, K., L. F. Koch, T. Tertel, et al. 2022. "Detailed Characterization of Small Extracellular Vesicles From Different Cell Types Based on Tetraspanin Composition by ExoView R100 Platform." *International Journal of Molecular Sciences* 23: 8544. https://doi.org/10.3390/ijms23158544.

Budayr, O. M., B. C. Miller, and J. Nguyen. 2025. "Harnessing Extracellular Vesicle-Mediated Crosstalk Between T Cells and Cancer Cells for Therapeutic Applications." *Journal of Control Release* 378: 266–280. https://doi.org/10.1016/j.jconrel.2024.12.011.

Cai, Z., F. Yang, L. Yu, et al. 2012. "Activated T Cell Exosomes Promote Tumor Invasion via Fas Signaling Pathway." *Journal of Immunology* 188: 5954–5961. https://doi.org/10.4049/jimmunol.1103466.

Cassioli, C., and C. T. Baldari. 2022. "The Expanding Arsenal of Cytotoxic T Cells." *Frontiers in Immunology* 13: 883010. https://doi.org/10.3389/fimmu.2022.883010.

Cassioli, C., N. Capitani, C. C. Staton, et al. 2025. "Activation-induced Thrombospondin-4 Works With Thrombospondin-1 to Build Cytotoxic Supramolecular Attack Particles." *PNAS* 122: e2413866122. https://doi.org/10.1073/pnas.2413866122.

Cespedes, P. F., A. Jainarayanan, L. Fernandez-Messina, et al. 2022. "T-cell Trans-synaptic Vesicles Are Distinct and Carry Greater Effector Content Than Constitutive Extracellular Vesicles." *Nature Communications* 13: 3460. https://doi.org/10.1038/s41467-022-31160-3.

Chang, H. F., H. Bzeih, C. Schirra, et al. 2016. "Endocytosis of Cytotoxic Granules Is Essential for Multiple Killing of Target Cells by T Lymphocytes." *Journal of Immunology* 197: 2473–2484. https://doi.org/10.4049/jimmunol.1600828.

Chang, H. F., C. Schirra, M. Ninov, et al. 2022. "Identification of Distinct Cytotoxic Granules as the Origin of Supramolecular Attack Particles in T Lymphocytes." *Nature Communications* 13: 1029. https://doi.org/10.1038/s41467-022-28596-y.

Chang, H. F., C. Schirra, V. Pattu, E. Krause, and U. Becherer. 2023. "Lytic Granule Exocytosis at Immune Synapses: Lessons From Neuronal Synapses." *Frontiers in Immunology* 14: 1177670. https://doi.org/10.3389/fimmu.2023.1177670.

Chitirala, P., H. F. Chang, P. Martzloff, et al. 2020. "Studying the Biology of Cytotoxic T Lymphocytes in Vivo With a Fluorescent Granzyme B-mTFP Knock-in Mouse." *Elife* 9: e58065. https://doi.org/10.7554/eLife.58065.

Crozat, K., K. Hoebe, S. Ugolini, et al. 2007. "Jinx, an MCMV Susceptibility Phenotype Caused by Disruption of Unc13d: A Mouse Model of Type 3 Familial Hemophagocytic Lymphohistiocytosis." *Journal of Experimental Medicine* 204: 853–863. https://doi.org/10.1084/jem.20062447.

Deutsch, E. W., N. Bandeira, Y. Perez-Riverol, et al. 2023. "The ProteomeXchange Consortium at 10 Years: 2023 Update." *Nucleic Acids Research* 51: D1539–D1548. https://doi.org/10.1093/nar/gkac1040.

Dudenhoffer-Pfeifer, M., C. Schirra, V. Pattu, et al. 2013. "Different Munc13 Isoforms Function as Priming Factors in Lytic Granule Release From Murine Cytotoxic T Lymphocytes." *Traffic (Copenhagen, Denmark)* 14: 798–809. https://doi.org/10.1111/tra.12074.

Estl, M., P. Blatt, X. Li, et al. 2020. "Various Stages of Immune Synapse Formation Are Differently Dependent on the Strength of the TCR Stimulus." *International Journal of Molecular Sciences* 21: 2475. https://doi.org/10.3390/ijms21072475.

Fecher-Trost, C., U. Wissenbach, A. Beck, et al. 2013. "The in Vivo TRPV6 Protein Starts at a Non-AUG Triplet, Decoded as Methionine, Upstream of Canonical Initiation at AUG." *Journal of Biological Chemistry* 288: 16629–16644. https://doi.org/10.1074/jbc.M113.469726.

Feldmann, J., I. Callebaut, G. Raposo, et al. 2003. "Munc13-4 is Essential for Cytolytic Granules Fusion and is Mutated in a Form of Familial Hemophagocytic Lymphohistiocytosis (FHL3)." *Cell* 115: 461–473. https://doi.org/10.1016/s0092-8674(03)00855-9.

Ghosh, D., T. K. Lim, A. Basu, J. C. Gross, and Q. Lin. 2025. "Quantitative Proteomics Identifies Possible Flow of Metastatic Cues Between Progressive Stages of Colorectal Cancer via Transfer of Ceramide-dependent Exosomal Cargoes." *Febs Journal* 292: 4516–4539. https://doi.org/10.1111/febs.17410.

Guay, C., J. K. Kruit, S. Rome, et al. 2019. "Lymphocyte-Derived Exosomal MicroRNAs Promote Pancreatic Beta Cell Death and May Contribute to Type 1 Diabetes Development." *Cell Metabolism* 29: 348–361 e346. https://doi.org/10.1016/j.cmet.2018.09.011.

Gustafsson, N., S. Culley, G. Ashdown, D. M. Owen, P. M. Pereira, and R. Henriques. 2016. "Fast Live-cell Conventional Fluorophore Nanoscopy With ImageJ Through Super-Resolution Radial Fluctuations." *Nature Communications* 7: 12471. https://doi.org/10.1038/ncomms12471.

Kaur, H., N. Xu, D. M. Doycheva, J. Malaguit, J. Tang, and J. H. Zhang. 2019. "Recombinant Slit2 Attenuates Neuronal Apoptosis via the Robo1-srGAP1 Pathway in a Rat Model of Neonatal HIE." *Neuropharmacology* 158: 107727. https://doi.org/10.1016/j.neuropharm.2019.107727.

Kim, H. Y., H. K. Min, H. W. Song, et al. 2022. "Delivery of human Natural Killer Cell-derived Exosomes for Liver Cancer Therapy: an in Vivo Study in Subcutaneous and Orthotopic Animal Models." *Drug Delivery* 29: 2897–2911. https://doi.org/10.1080/10717544.2022.2118898.

Kotelevets, L., and E. Chastre. 2021. "A New Story of the Three Magi: Scaffolding Proteins and lncRNA Suppressors of Cancer." *Cancers (Basel)* 13: 4264. https://doi.org/10.3390/cancers13174264.

Kowal, J., G. Arras, M. Colombo, et al. 2016. "Proteomic Comparison Defines Novel Markers to Characterize Heterogeneous Populations of

Extracellular Vesicle Subtypes." *PNAS* 113: E968–977. https://doi.org/10.1073/pnas.1521230113.

Laine, R. F., H. S. Heil, S. Coelho, et al. 2023. "High-fidelity 3D Live-cell Nanoscopy Through Data-driven Enhanced Super-resolution Radial Fluctuation." *Nature Methods* 20: 1949–1956. https://doi.org/10.1038/s41592-023-02057-w.

Lettau, M., M. Dietz, K. Dohmen, M. Leippe, D. Kabelitz, and O. Janssen. 2019. "Granulysin Species Segregate to Different Lysosome-related Effector Vesicles (LREV) and Get Mobilized by either Classical or Non-classical Degranulation." *Molecular Immunology* 107: 44–53. https://doi.org/10.1016/j.molimm.2018.12.031.

Lettau, M., and O. Janssen. 2021. "Intra- and Extracellular Effector Vesicles from Human T and NK Cells: Same-Same, but Different?" *Frontiers in Immunology* 12: 804895. https://doi.org/10.3389/fimmu.2021.804895.

Li, L., S. M. Jay, Y. Wang, S. W. Wu, and Z. Xiao. 2017. "IL-12 Stimulates CTLs to Secrete Exosomes Capable of Activating Bystander CD8(+) T Cells." *Scientific Reports* 7: 13365. https://doi.org/10.1038/s41598-017-14000-z.

Li, Y., Q. Yang, D. Li, W. Li, and W. Men. 2025. "Exosomes: Key Messengers Mediating the Interaction between Tumor Cells and CD8(+) T Cells in the Tumor Microenvironment." *International Journal of Nanomedicine* 20: 653–667. https://doi.org/10.2147/IJN.S502363.

Liu, C., D. Liu, S. Wang, L. Gan, X. Yang, and C. Ma. 2023. "Identification of the SNARE Complex That Mediates the Fusion of Multivesicular Bodies With the Plasma Membrane in Exosome Secretion." *Journal of Extracellular Vesicles* 12: e12356. https://doi.org/10.1002/jev2.12356.

Liu, Y., C. Schirra, L. Edelmann, et al. 2010. "Two Distinct Secretory Vesicle-priming Steps in Adrenal Chromaffin Cells." *Journal of Cell Biology* 190: 1067–1077. https://doi.org/10.1083/jcb.201001164.

Lopez, J. A., O. Susanto, M. R. Jenkins, et al. 2013. "Perforin Forms Transient Pores on the Target Cell Plasma Membrane to Facilitate Rapid Access of Granzymes During Killer Cell Attack." *Blood* 121: 2659–2668. https://doi.org/10.1182/blood-2012-07-446146.

Lu, S., Z. Sun, L. Liu, et al. 2022. "Tumor-Derived Exosomes Regulate Apoptosis of CD45(+)EpCAM(+) Cells in Lung Cancer." *Frontiers in Immunology* 13: 903882. https://doi.org/10.3389/fimmu.2022.903882.

Lunavat, T. R., L. Cheng, D. K. Kim, et al. 2015. "Small RNA Deep Sequencing Discriminates Subsets of Extracellular Vesicles Released by Melanoma Cells–Evidence of Unique microRNA Cargos." *RNA Biology* 12: 810–823. https://doi.org/10.1080/15476286.2015.1056975.

Mahmood, A., Z. Otruba, A. W. Weisgerber, et al. 2023. "Exosome Secretion Kinetics Are Controlled by Temperature." *Biophysical Journal* 122: 1301–1314. https://doi.org/10.1016/j.bpj.2023.02.025.

Maier, J. K., Z. Lahoua, N. H. Gendron, et al. 2002. "The Neuronal Apoptosis Inhibitory Protein Is a Direct Inhibitor of Caspases 3 and 7." *Journal of Neuroscience* 22: 2035–2043. https://doi.org/10.1523/JNEUROSCI.22-06-02035.2002.

Martina, J. A., X. S. Wu, M. Catalfamo, T. Sakamoto, C. Yi, and J. A. Hammer 3rd. 2011. "Imaging of Lytic Granule Exocytosis in CD8+ Cytotoxic T Lymphocytes Reveals a Modified Form of Full Fusion." *Cellular Immunology* 271: 267–279. https://doi.org/10.1016/j.cellimm.2011.07.004.

McKenzie, B., R. Khazen, and S. Valitutti. 2022. "Greek Fire, Poison Arrows, and Scorpion Bombs: How Tumor Cells Defend against the Siege Weapons of Cytotoxic T Lymphocytes." *Frontiers in Immunology* 13: 894306. https://doi.org/10.3389/fimmu.2022.894306.

Menager, M. M., G. Menasche, M. Romao, et al. 2007. "Secretory Cytotoxic Granule Maturation and Exocytosis Require the Effector Protein hMunc13-4." *Nature Immunology* 8: 257–267. https://doi.org/10.1038/ni1431.

Messenger, S. W., S. S. Woo, Z. Sun, and T. F. J. Martin. 2018. "A Ca(2+)-stimulated Exosome Release Pathway in Cancer Cells Is Regulated by Munc13-4." *Journal of Cell Biology* 217: 2877–2890. https://doi.org/10.1083/jcb.201710132.

Metzelaar, M. J., P. L. Wijngaard, P. J. Peters, J. J. Sixma, H. K. Nieuwenhuis, and H. C. Clevers. 1991. "CD63 antigen. A Novel Lysosomal Membrane Glycoprotein, Cloned by a Screening Procedure for Intracellular Antigens in Eukaryotic Cells." *Journal of Biological Chemistry* 266: 3239–3245.

Monleon, I., M. J. Martinez-Lorenzo, L. Monteagudo, et al. 2001. "Differential Secretion of Fas Ligand- or APO2 Ligand/TNF-related Apoptosis-inducing Ligand-Carrying Microvesicles During Activation-induced Death of human T Cells." *Journal of Immunology* 167: 6736–6744. https://doi.org/10.4049/jimmunol.167.12.6736.

Morelli, A. E., A. T. Larregina, W. J. Shufesky, et al. 2004. "Endocytosis, Intracellular Sorting, and Processing of Exosomes by Dendritic Cells." *Blood* 104: 3257–3266. https://doi.org/10.1182/blood-2004-03-0824.

Nagata, S., and M. Tanaka. 2017. "Programmed Cell Death and the Immune System." *Nature Reviews Immunology* 17: 333–340. https://doi.org/10.1038/nri.2016.153.

Pachitariu, M., and C. Stringer. 2022. "Cellpose 2.0: How to Train Your Own Model." *Nature Methods* 19: 1634–1641. https://doi.org/10.1038/s41592-022-01663-4.

Perez-Hernandez, D., C. Gutierrez-Vazquez, I. Jorge, et al. 2013. "The Intracellular Interactome of Tetraspanin-enriched Microdomains Reveals Their Function as Sorting Machineries Toward Exosomes." *Journal of Biological Chemistry* 288: 11649–11661. https://doi.org/10.1074/jbc.M112.445304.

Perez-Riverol, Y., C. Bandla, D. J. Kundu, et al. 2025. "The PRIDE Database at 20 Years: 2025 Update." *Nucleic Acids Research* 53: D543–D553. https://doi.org/10.1093/nar/gkae1011.

Perez-Riverol, Y., Q. W. Xu, R. Wang, et al. 2016. "PRIDE Inspector Toolsuite: Moving toward a Universal Visualization Tool for Proteomics Data Standard Formats and Quality Assessment of ProteomeXchange Datasets." *Molecular & Cellular Proteomics* 15: 305–317. https://doi.org/10.1074/mcp.O115.050229.

Peters, P. J., J. Borst, V. Oorschot, et al. 1991. "Cytotoxic T Lymphocyte Granules Are Secretory Lysosomes, Containing both Perforin and Granzymes." *Journal of Experimental Medicine* 173: 1099–1109. https://doi.org/10.1084/jem.173.5.1099.

Prager, I., C. Liesche, H. van Ooijen, et al. 2019. "NK Cells Switch From Granzyme B to Death Receptor-mediated Cytotoxicity During Serial Killing." *Journal of Experimental Medicine* 216: 2113–2127. https://doi.org/10.1084/jem.20181454.

Quintana, A., M. Pasche, C. Junker, et al. 2011. "Calcium Microdomains at the Immunological Synapse: How ORAI Channels, Mitochondria and Calcium Pumps Generate Local Calcium Signals for Efficient T-cell Activation." *Embo Journal* 30: 3895–3912. https://doi.org/10.1038/emboj.2011.289.

Rana, S., S. Yue, D. Stadel, and M. Zoller. 2012. "Toward Tailored Exosomes: the Exosomal Tetraspanin Web Contributes to Target Cell Selection." *International Journal of Biochemistry & Cell Biology* 44: 1574–1584. https://doi.org/10.1016/j.biocel.2012.06.018.

Raposo, G., and W. Stoorvogel. 2013. "Extracellular Vesicles: Exosomes, Microvesicles, and Friends." *Journal of Cell Biology* 200: 373–383. https://doi.org/10.1083/jcb.201211138.

Reddy, V. S., S. K. Madala, J. Trinath, and G. B. Reddy. 2018. "Extracellular Small Heat Shock Proteins: Exosomal Biogenesis and Function." *Cell Stress & Chaperones* 23: 441–454. https://doi.org/10.1007/s12192-017-0856-z.

Rydland, A., F. Heinicke, S. T. Flam, M. D. Mjaavatten, and B. A. Lie. 2023. "Small Extracellular Vesicles Have Distinct CD81 and CD9 Tetraspanin Expression Profiles in Plasma From Rheumatoid Arthritis Patients." *Clinical and Experimental Medicine* 23: 2867–2875. https://doi.org/10.1007/s10238-023-01024-1.

Schirra, C., N. Alawar, U. Becherer, and H. F. Chang. 2023. "Separation of Single Core and Multicore Lytic Granules by Subcellular Fractionation and Immunoisolation." *Methods in Molecular Biology* 2654: 159–167. https://doi.org/10.1007/978-1-0716-3135-5_11.

Seo, N., Y. Shirakura, Y. Tahara, et al. 2018. "Activated CD8(+) T Cell Extracellular Vesicles Prevent Tumour Progression by Targeting of Lesional Mesenchymal Cells." *Nature Communications* 9: 435. https://doi.org/10.1038/s41467-018-02865-1.

Shaib, A. H., A. A. Chouaib, R. Chowdhury, et al. 2024. "One-Step Nanoscale Expansion Microscopy Reveals Individual Protein Shapes." *Nature Biotechnology* 43: 1539–1547. https://doi.org/10.1038/s41587-024-02431-9.

Sovunjov, E., Z. S. Halbutogullari, G. Gacar, A. Ozturk, G. Duruksu, and Y. Yazir. 2023. "Examining the Effect of Activated Cytotoxic (CD8(+)) T-cell Exosomes to the Lung Cancer." *Medical Oncology* 40: 359. https://doi.org/10.1007/s12032-023-02198-0.

Stinchcombe, J. C., E. Majorovits, G. Bossi, S. Fuller, and G. M. Griffiths. 2006. "Centrosome Polarization Delivers Secretory Granules to the Immunological Synapse." *Nature* 443: 462–465. https://doi.org/10.1038/nature05071.

Sutton, V. R., A. J. Brennan, S. Ellis, et al. 2016. "Serglycin Determines Secretory Granule Repertoire and Regulates Natural Killer Cell and Cytotoxic T Lymphocyte Cytotoxicity." *Febs Journal* 283: 947–961. https://doi.org/10.1111/febs.13649.

Tauro, B. J., D. W. Greening, R. A. Mathias, S. Mathivanan, H. Ji, and R. J. Simpson. 2013. "Two Distinct Populations of Exosomes Are Released From LIM1863 Colon Carcinoma Cell-derived Organoids." *Molecular & Cellular Proteomics* 12: 587–598. https://doi.org/10.1074/mcp.M112.021303.

Thery, C., S. Amigorena, G. Raposo, and A. Clayton. 2006. "Isolation and Characterization of Exosomes From Cell Culture Supernatants and Biological Fluids." Current Protocols in Cell Biology Chapter 3:Unit 3 22. https://doi.org/10.1002/0471143030.cb0322s30.

Toth, E. A., L. Turiak, T. Visnovitz, et al. 2021. "Formation of a Protein Corona on the Surface of Extracellular Vesicles in Blood Plasma." *Journal of Extracellular Vesicles* 10: e12140. https://doi.org/10.1002/jev2.12140.

Uhl, L. F. K., H. Cai, S. L. Oram, et al. 2023. "Interferon-gamma Couples CD8(+) T Cell Avidity and Differentiation During Infection." *Nature Communications* 14: 6727. https://doi.org/10.1038/s41467-023-42455-4.

Valadi, H., K. Ekstrom, A. Bossios, M. Sjostrand, J. J. Lee, and J. O. Lotvall. 2007. "Exosome-mediated Transfer of mRNAs and microRNAs Is a Novel Mechanism of Genetic Exchange Between Cells." *Nature Cell Biology* 9: 654–659. https://doi.org/10.1038/ncb1596.

van Niel, G., S. Charrin, S. Simoes, et al. 2011. "The Tetraspanin CD63 Regulates ESCRT-independent and -dependent Endosomal Sorting During Melanogenesis." *Developmental Cell* 21: 708–721. https://doi.org/10.1016/j.devcel.2011.08.019.

van Niel, G., G. D'Angelo, and G. Raposo. 2018. "Shedding Light on the Cell Biology of Extracellular Vesicles." *Nature Reviews Molecular Cell Biology* 19: 213–228. https://doi.org/10.1038/nrm.2017.125.

Verweij, F. J., M. P. Bebelman, C. R. Jimenez, et al. 2018. "Quantifying Exosome Secretion From Single Cells Reveals a Modulatory Role for GPCR Signaling." *Journal of Cell Biology* 217: 1129–1142. https://doi.org/10.1083/jcb.201703206.

Vij, N., L. Roberts, S. Joyce, and S. Chakravarti. 2005. "Lumican Regulates Corneal Inflammatory Responses by Modulating Fas-Fas Ligand Signaling." *Investigative Ophthalmology & Visual Science* 46: 88–95. https://doi.org/10.1167/iovs.04-0833.

Weigelin, B., A. T. den Boer, E. Wagena, et al. 2021. "Cytotoxic T Cells Are Able to Efficiently Eliminate Cancer Cells by Additive Cytotoxicity." *Nature Communications* 12: 5217. https://doi.org/10.1038/s41467-021-25282-3.

Welsh, J. A., D. C. I. Goberdhan, L. O'Driscoll, et al. 2024. "Minimal Information for Studies of Extracellular Vesicles (MISEV2023): from Basic to Advanced Approaches." *Journal of Extracellular Vesicles* 13: e12404. https://doi.org/10.1002/jev2.12404.

Wu, S. W., L. Li, Y. Wang, and Z. Xiao. 2019. "CTL-Derived Exosomes Enhance the Activation of CTLs Stimulated by Low-Affinity Peptides." *Frontiers in Immunology* 10: 1274. https://doi.org/10.3389/fimmu.2019.01274.

Xu, R., D. W. Greening, A. Rai, H. Ji, and R. J. Simpson. 2015. "Highly-purified Exosomes and Shed Microvesicles Isolated From the human Colon Cancer Cell Line LIM1863 by Sequential Centrifugal Ultrafiltration Are Biochemically and Functionally Distinct." *Methods (San Diego, California)* 87: 11–25. https://doi.org/10.1016/j.ymeth.2015.04.008.

Yin, Z., H. Zhang, K. Zhao, et al. 2024. "Zebrafish FKBP5 Facilitates Apoptosis and SVCV Propagation by Suppressing NF-kappaB Signaling Pathway." *Fish & Shellfish Immunology* 155: 110021. https://doi.org/10.1016/j.fsi.2024.110021.

Zhang, L., Y. Meng, Y. An, X. Yang, F. Wei, and X. Ren. 2024. "The Antitumor Effect of Extracellular Vesicles Derived From Cytokine-activated CD8+ T Cells." *Journal of Leukocyte Biology* 116: 1033–1044. https://doi.org/10.1093/jleuko/qiae117.

Zhou, W. J., J. Zhang, F. Xie, et al. 2021. "CD45RO(-)CD8(+) T Cell-Derived Exosomes Restrict Estrogen-driven Endometrial Cancer Development via the ERbeta/miR-765/PLP2/Notch Axis." *Theranostics* 11: 5330–5345. https://doi.org/10.7150/thno.58337.

Zuccato, E., E. J. Blott, O. Holt, et al. 2007. "Sorting of Fas Ligand to Secretory Lysosomes Is Regulated by Mono-ubiquitylation and Phosphorylation." *Journal of Cell Science* 120: 191–199. https://doi.org/10.1242/jcs.03315.

Dustin, M. L., and K. Choudhuri. 2016. "Signaling and Polarized Communication Across the T Cell Immunological Synapse." *Annual Review of Cell and Developmental Biology* 32: 303–325. https://doi.org/10.1146/annurev-cellbio-100814-125330.

Kabanova, A., V. Zurli, and C. T. Baldari. 2018. "Signals Controlling Lytic Granule Polarization at the Cytotoxic Immune Synapse." *Frontiers in Immunology* 9: 307. https://doi.org/10.3389/fimmu.2018.00307.

American Veterinary Medical Association. 2007. "AVMA Guidelines on Euthanasia." (Formerly the Report of the AVMA Panel on Euthanasia). https://grants.nih.gov/grants/olaw/Euthanasia2007.pdf.

Matti, U., V. Pattu, M. Halimani, et al. 2013. "Synaptobrevin2 is the v-SNARE required for cytotoxic T-lymphocyte lytic granule fusion." *Nat Commun* 4: 1439. https://doi.org/10.1038/ncomms2467.

Supporting Information

Additional supporting information can be found online in the Supporting Information section.

Supplementary Information: jev270239-sup-0001-SuppMat.docx **Supplementary Table**: jev270239-sup-0002-TableS2.xlsx **Supplementary Table**: jev270239-sup-0003-TableS3.xlsx **Supplementary Table**: jev270239-sup-0004-TableS4.xlsx